UNIVERSIDADE FEDERAL DE PERNAMBUCO
CENTRO DE CIÊNCIAS EXATAS E DA NATUREZA
PROGRAMA DE PÓS-GRADUAÇÃO EM FÍSICA

RAISSA PENHA MACHADO

Faraday rotation and four wave mixing in rubidium vapour with intense fields

Recife

2024

RAISSA PENHA MACHADO

Faraday rotation and four wave mixing in rubidium vapour with intense fields

Dissertação apresentada ao Programa de Pós-Graduação em Física da Universidade Federal de Pernambuco, como requisito parcial para a obtenção do título de Mestre em Física.

Área de Concentração: Óptica

Orientador (a): Sandra Sampaio Vianna

Recife

2024

.Catalogação de Publicação na Fonte. UFPE - Biblioteca Central

Machado, Raissa Penha.
   Faraday rotation and four wave mixing in rubidium vapour with intense fields / Raissa Penha Machado. - Recife, 2024.
   61f.: il.

   Dissertação (Mestrado) - Universidade Federal de Pernambuco, Centro de Ciências Exatas e da Natureza, Programa de Pós-Graduação em Física, 2024.
   Orientação: Sandra Sampaio Vianna.

   1. Faraday effect; 2. Four-wave mixing; 3. Nonlinear optics; 4. Atomic vapor. I. Vianna, Sandra Sampaio. II. Título.

UFPE-Biblioteca Central

RAISSA PENHA MACHADO

ROTAÇÃO DE FARADAY E MISTURA DE QUATRO ONDAS EM VAPOR DE RUBÍDIO COM CAMPOS INTENSOS

Dissertação apresentada ao Programa de Pós-Graduação em Física da Universidade Federal de Pernambuco, como requisito parcial para a obtenção do título de Mestra em Física.

Data de aprovação: 19/08/2024.

BANCA EXAMINADORA

_____

Profa. Dra. Sandra Sampaio Vianna
Orientadora
Universidade Federal de Pernambuco

_____

Prof. Dr. José Wellington Rocha Tabosa
Examinador Interno
Universidade Federal de Pernambuco

_____

Prof. Dr. Romain Pierre Marcel Bachelard
Examinador Externo
Universidade Federal de São Carlos

A minha avó Anália.

ACKNOWLEDGEMENTS

To my mother and grandmother, I thank for the support and stimulus that they have always given me that was essential for me to achieve this work.

For my sisters and friends, I thank you for the fun moments you have given me that allowed me to pass through this phase more lightly.

I thank my professor Sandra for giving so many lessons, not only in physics, but also in life in general.

To my dogs I thank for their emotional support.

Finally, I would like to thank FACEPE, CAPES and CNPq for their financial support

"Maybe I made a mistake yesterday, but yesterday's me is still me. I am who I am today, with all my faults. Tomorrow I might be a tiny bit wiser, and that's me, too. These faults and mistakes are what I am, making up the brightest stars in the constellation of my life. I have come to love myself for who I was, who I am, and who I hope to become." — Kim Namjoong

ABSTRACT

The study of nonlinear interactions of light with an atomic sample has been fundamental for the understanding of several problems. In particular, it is well known that different processes can occur simultaneously and interfere with each other. In this work we investigate the frequency dependence of two processes: degenerated four-wave mixing and Faraday rotation, using a sample of hot rubidium atoms as a nonlinear medium. We use a single cw laser to generate two input laser beams with linear and orthogonal polarizations, labeled by their wave vectors $\vec{k_a}$ and $\vec{k_b}$. These two beams interact with the sample, generating two four-wave mixing (FWM) signals in the $2\vec{k_a} - \vec{k_b}$ and $2\vec{k_b} - \vec{k_a}$ directions. This is a degenerated process with the input and output beams tuned in the D2 line, $5S_{1/2} \rightarrow 5P_{3/2}$ transition, of Rb. We focused our studies in one of the FWM signals,$2\vec{k_b} - \vec{k_a}$, and analyzed the rotation of polarization of the transmitted beam, $\vec{k_b}$, after it passed through the sample. Measurements were made for three temperatures and different intensity ratios between the two input beams. For high temperatures and low probe beam intensity, I_a, we observe a large Faraday rotation effect in the $\vec{k_b}$ pump beam while the FWM signal presents a Doppler-type spectrum. As the probe beam intensity increases, reaching the same intensity as the b beam, a peak structure appears in the FWM signal spectra, while the Faraday rotation effect appears to diminish due to the presence of an intense a beam.

Keywords: Faraday effect. Four-wave mixing. Nonlinear optics. Atomic vapor.

RESUMO

O estudo de interações não lineares da luz com vapores atômicos tem sido fundamental para a compreensão de vários problemas. Em particular, sabe-se que diferentes processos podem acontecer simultaneamente e interferir entre si. Neste trabalho investigamos a dependência com a frequência de dois processos: mistura de quatro ondas degenerada e rotação da polarização devido ao efeito Faraday. Usamos um único laser cw para gerar dois feixes de entrada com polarizações lineares e ortogonais, designadas por seus vetores de onda $\vec{k_a}$ e $\vec{k_b}$. Estes dois feixes interagem com a amostra, gerando dois sinais de mistura de quatro ondas, nas direções $2\vec{k_a} - \vec{k_b}$ e $2\vec{k_b} - \vec{k_a}$. Este é um processo degenerado com os feixes de entrada e saída sintonizados na linha D2, na transição $5S_{1/2} \rightarrow 5P_{3/2}$, do rubídio. Nós focamos nossos estudos em um dos sinais, $2\vec{k_b} - \vec{k_a}$, e analisamos a rotação da polarização do feixe transmitido, $\vec{k_b}$, após este passar pela amostra. As medidas foram feitas em três temperaturas diferentes e com razões de intensidades entre os feixes de entrada variadas. Para altas temperaturas e baixa intensidade do feixe de prova, I_a, observamos um grande efeito de rotação da polarização no feixe de bombeio, I_b, enquanto o sinal de mistura de quatro ondas apresenta um espectro do tipo Doppler. Quando a intensidade do feixe de prova cresce, alcançando a mesma intensidade do feixe de bombeio, uma estrutura de picos aparece no espectro de mistura de quatro onda, enquanto a rotação da polarização do feixe b parece diminuir na presença do feixe de prova.

Palavras-chaves: Efeito Faraday. Mistura de quatro ondas. Óptica não linear. Vapor atômico.

LIST OF FIGURES

CONTENTS

1 INTRODUCTION

Nonlinear optics is an interesting area that looks into optical behaviors when a material doesn't respond linearly to a strong electromagnetic field, instead involves higher powers. This subject has made substantial advances, impacting fields like telecommunications and quantum optics. Its roots go back to mid-20th century papers, gaining momentum after the invention of lasers in 1960 (MAIMAN, 1960), which allowed researchers to experimentally test concepts like two-photon excitation, second harmonic generation and four-wave mixing (FWM).

Four-wave mixing is a third-order nonlinear effect where two input electromagnetic waves interact with a nonlinear medium to generate new waves at different frequencies (ARMSTRONG et al., 1962).While researchers have explored this phenomenon in various nonlinear media, we are particularly interested in its manifestation in atomic vapors. This phenomenon has been observed in systems that are relatively simple, with two and three energy levels, in different configurations like lambda, V and cascade. Regarding recent FWM applications connected to the studies in this work, notable examples include the generation of quantum-correlated beams (MA et al., 2018), quantum memory storage (CHOPINAUD et al., 2018), transfer of orbital angular momentum among light beams (OFFER et al., 2018) and the reduction of paraxial light diffraction (KATZIR; RON; FIRSTENBERG, 2015).

In the year 1846, Michael Faraday achieved a significant breakthrough by uncovering a remarkable phenomenon. His discovery showed that when light propagates through different materials under the influence of a magnetic field along its axis, the plane of the light polarization undergoes a rotation. This discovery, referred to as the Faraday effect, was groundbreaking as it represented the initial recognition of a magneto-optic phenomenon (FARADAY; COLLIN; LIBRARY, 1846). Some of the Faraday effect applications involve magnometry and optical isolation.

In this work, our focus is on two intriguing optical phenomena: the Faraday effect and the four-wave mixing process. Initially, our primary goal is centered around the exploration of four-wave mixing. As some experiments, involving Hermite-Gauss and Laguerre-Gauss modulated beams, were being carried at the laboratory a noteworthy observation emerged: we detected light propagating in the direction of the transmitted beam, with polarization perpendicular to that of the incident beam. Delving into the origins of this phenomenon, we noted that the use of a magnetic shield led to the disappearance of this light with perpendicular polarization.

Coupled with the fact that the incoming beam is linearly polarized we were led to the conclusion that the observed light with the unexpected polarization is a consequence of the Faraday Effect.

Further on this Introduction we are going to give some important characteristics of the rubidium atomic structure, since it is the atomic element used as the nonlinear medium. In the sequence we are going to talk about the Zeeman effect, needed to explain the Faraday rotation.

In chapter 2 we will give an overview of the Faraday effect and a brief explanation about the saturated absorption spectroscopy (SAS) experiment, which is used to control and monitor the laser frequency. Next, we will explain the Faraday's rotation experiment and show our experimental results from which we estimated the rotation angle.

In chapter 3 our focus is the four wave mixing (FWM) experiment. We give a short introduction to the FWM process, explain our experimental setup and then show our results. In chapter 4 we present our conclusions and perspectives.

1.1 RUBIDIUM

For Faraday rotation and four wave mixing experiments we use rubidium vapour as the nonlinear medium. Rubidium is an alkali metal that is commonly used in optical experiments. In the experiments that we performed we focused in the transition $5S_{1/2}$ - fundamental state - to the $5P_{3/2}$ excited state.

In nature, two most common isotopes of rubidium are found: ^{85}Rb, constituting 72% with nuclear spin I $= 5/2$, and ^{87}Rb, constituting 28% with nuclear spin I $= 3/2$. The values of nuclear spin cause the $5S_{1/2}$ state to split into two levels, and the $5P_{3/2}$ state into four hyperfine levels, as shown in the energy level diagram presented in figures 1 and 2. In our experiments, we used a rubidium vapor cell at its natural concentration.

Figure 1 – Level diagram of ^{85}Rb, D2 line

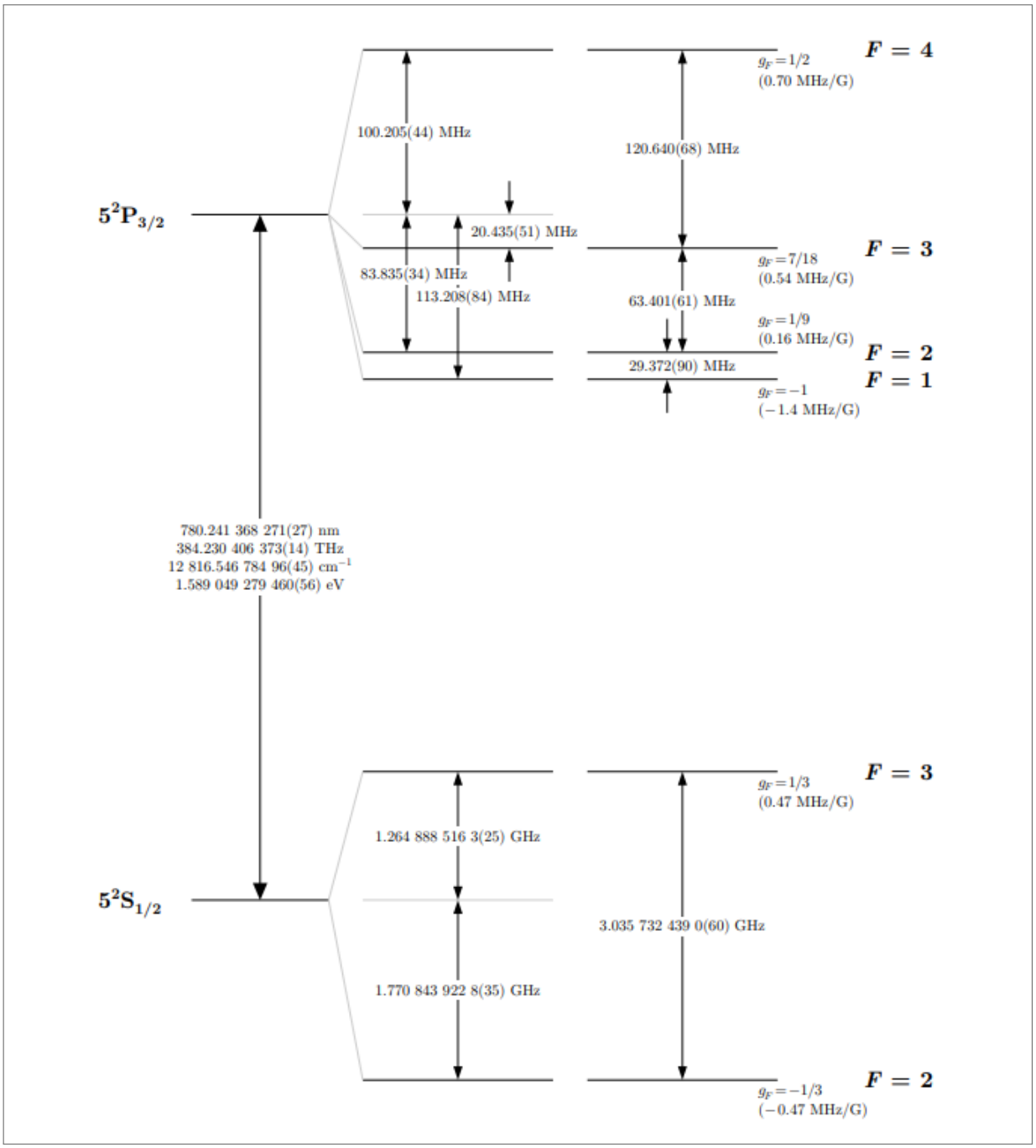

Source: taken from reference (STECK, 2007)

Figure 2 – Level diagram of ^{87}Rb, D2 line

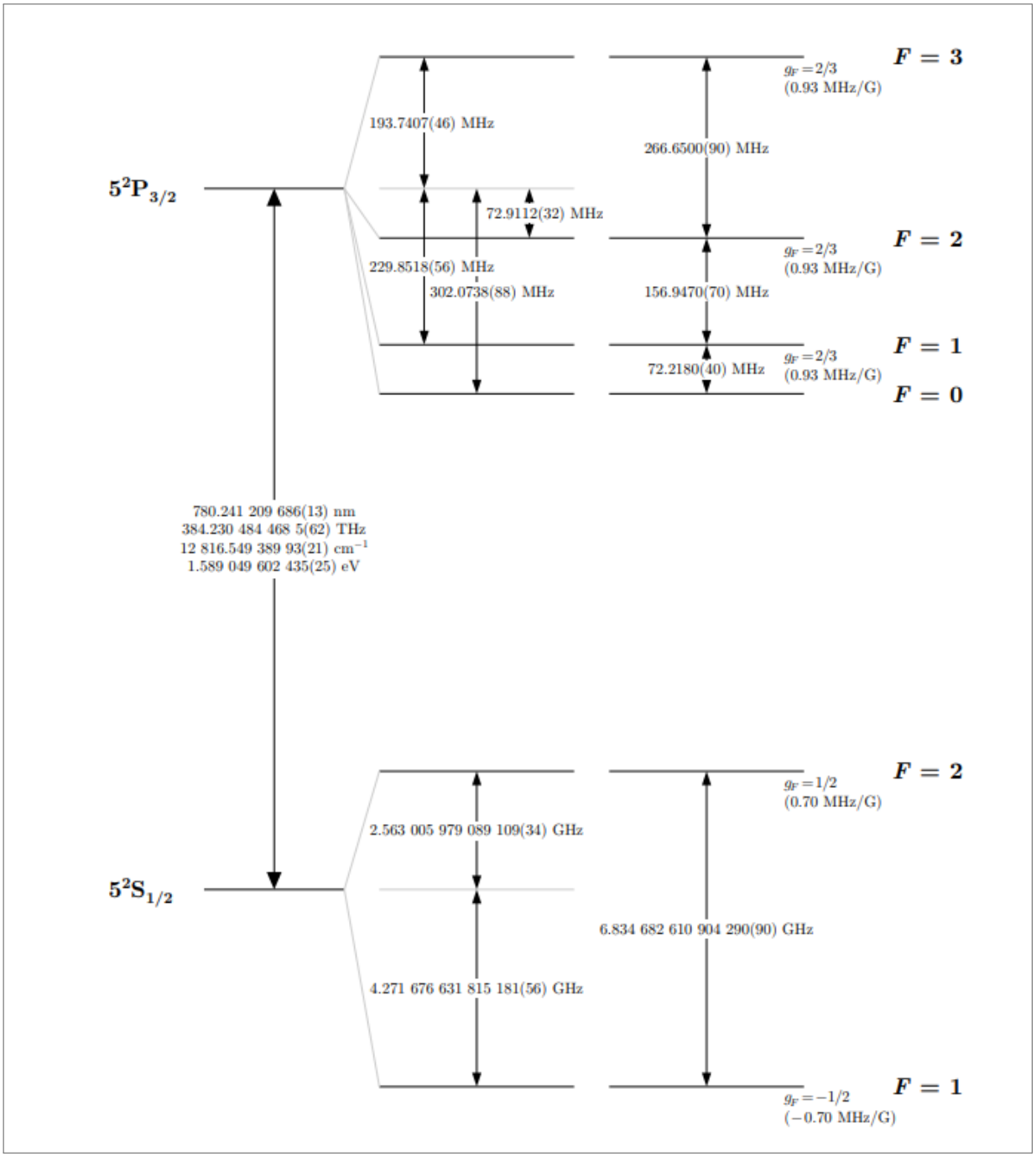

Source: taken from reference (STECK, 2003)

1.2 WEAK-FIELD ZEEMAN EFFECT

The presence of an external magnetic field causes a shift in the energy levels of an atom, due to a magnetic dipole interaction. This phenomenon is known as the Zeeman effect. This effect depends strongly on the strength of the external magnetic field. Since we are going to deal only with the Earth magnetic field, with order of magnitude of 0.5 G, in this text we will focus in the weak field regime.

When the energy shift caused by the magnetic field is considerably smaller than the hyperfine splittings neither I, the nuclear spin, nor J, the total angular momentum, are individually conserved but their sum F is. Therefore F is a good quantum number. We can then write the Hamiltonian term that describes the interaction with the external magnetic field as (FOOT, 2004):

$$H_Z^{'} = -\vec{\mu_F} \cdot \vec{B_{ext}}, \tag{1.1}$$

where μ_F is the total magnetic moment. Taking the $\vec{B_{ext}}$ parallel to the z direction we can write this term as:

$$H_z^{'} = \mu_B g_F F_z B_z,$$

where μ_B is the Bohr magneton, g_F is the hyperfine Landé g-factor, F_z is the component of the total angular momentum along the z-direction, and B_z represents the z-component of the external magnetic field.

Solving the hamiltonian to the lowest order will give us the energy splitting from the hyperfine sublevels (STECK, 2003):

$$\Delta E = \mu_B g_F m_F B_z. \tag{1.2}$$

The splittings depends on m_F, the magnetic quantum number associated with the total angular momentum F, so the energy will be higher for positive m_F and lower for negative m_F. This shift of the energy levels with dependence on the values of m_F will be important to explain the Faraday rotation, as we will see in the next chapter.

2 THE FARADAY EFFECT

This chapter is dedicated to the Faraday rotation. First, we give a small theoretical introduction to the Faraday effect and then we explain our experiment setup, including the saturated absorption spectroscopy. Finally, we show our results and estimate the rotation angle.

The Faraday effect denotes the rotation of light polarization during its propagation through a material to which a magnetic field is applied. Light with linear polarization can be considered as a superposition of right- and left-circularly polarized components interacting differently with the material. Without a magnetic field, each of the components will have the same resonance frequency. However, when a magnetic field is applied, there is a shift in the energy levels due to the Zeeman effect. As a result the resonance frequency is changed and one component of the linearly polarized light is slowed more than the other. This creates a phase shift between the two orthogonal components. When they recombine, the resulting light is again linearly polarized, but with a rotated polarization direction. We will see that the actual amount and direction depend both on material properties and on the relative strength of the magnetic field. The angle of rotation is given by:

$$\phi = VB_zL, \tag{2.1}$$

where V is the Verdet constant, B_z is the longitudinal magnetic field and L is the length of the sample (WELLER et al., 2012). This was the first effect discovered to relate light, electricity, and magnetism.

The Verdet constant plays an important role in this effect, representing the material-specific factor determining the extent of rotation induced by the magnetic field. Notably, materials such as low-density alkali vapors (e.g., rubidium and cesium) exhibit a Faraday effect with exceptionally high Verdet constants compared to other substances. For rubidium, the Verdet constant is $V = 1.4 \times 10^3$ rad $\mathsf{T}^{-1}\mathsf{m}^{-1}$, in contrast, the Verdet constant for YIG is only $V = 3.8 \times 10^2$ rad $\mathsf{T}^{-1}\mathsf{m}^{-1}$ and for TGG is even smaller, $V = 82$ rad $\mathsf{T}^{-1}\mathsf{m}^{-1}$. (WELLER et al., 2012). This constant can, however, be greater in cooled atoms, as observed in (LABEYRIE; MINIATURA; KAISER, 2001).

The Macaluso-Corbino effect is a specific form of the Faraday effect observed near resonance absorption lines. This phenomenon becomes apparent in a specific atomic transition, like the $F = 1 \rightarrow F' = 0$ transition. Without a magnetic field, the $m_F = \pm 1$ sublevels are

degenerate, and the optical resonance frequencies for circular polarizations ($\sigma+$ and $\sigma-$) align. (WILSON, 2020) However, introducing a magnetic field leads to Zeeman shifts, as seen in figure 3. These shifts depend on m_F, so for positive m_F we have an increase and for negative m_F we have a decrease in the energy level. When this happens, each component of linear polarization, σ^+ and σ^- sees a distinct refractive index, n_+ and n_-, as figure 4 shows, and therefore each has a different velocity in the medium, leading to a rotation in the linearly polarized light. The angle of rotation can also be expressed by (BUDKER et al., 2002):

$$\phi = \pi(n_+ - n_-)\frac{L}{\lambda}, \tag{2.2}$$

where λ is the light wavelength, this is for the linear Faraday effect which depends linearly on B (for small magnetic fields).

Figure 3 – In the presence of a longitudinal magnetic field, the Zeeman sublevels of the ground state experience an energy shift of $g\mu BM$. Consequently, this results in a disparity in resonance frequencies between left-circularly polarized $(\sigma+)$ and right-circularly polarized $(\sigma-)$ light.

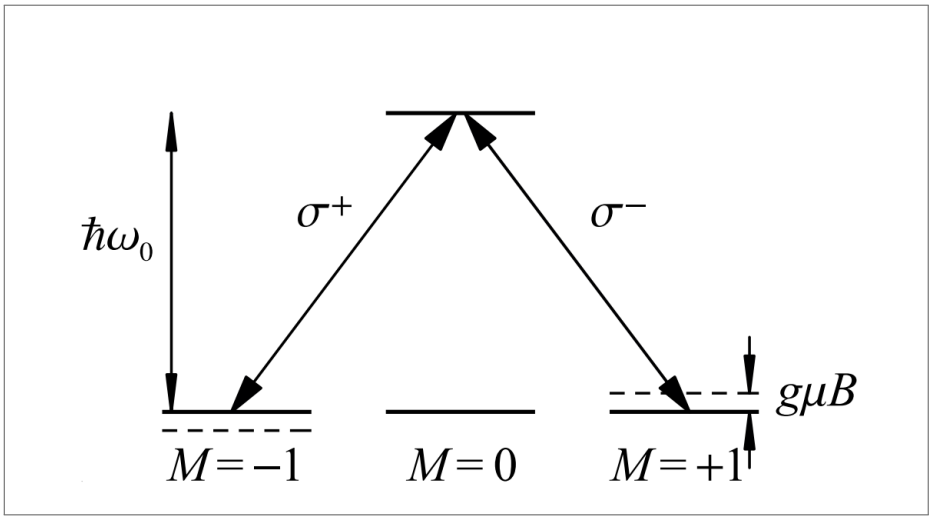

Source: taken from reference (BUDKER et al., 2002)

To calculate the rotation angle, we can use the density matrix formalism. From equation 2.2 we can relate the rotation angle to the refraction index and thus to the susceptibility (BOYD, 2008):

$$n^{\pm} = \sqrt{1 + Re(\chi^{\pm})}. \tag{2.3}$$

For $\chi \ll 1$ we can approximate the rotation angle, in first order, to:

$$\phi \approx \frac{\pi}{2\lambda} Re(\chi^+ - \chi^-)L, \tag{2.4}$$

where the susceptibility is related to the density matrix through (BOYD et al., 1981):

$$\chi_{ij} = \frac{2N\mu_{ij}}{\epsilon_0 E}\rho_{ij}. \tag{2.5}$$

where N is the number density of atoms. The Liouville equation gives us the relation between the density matrix and the Hamiltonian of the problem. Considering the electric dipole approximation for the interaction of a two level system $|1\rangle$ to $|2\rangle$ and an electromagnetic wave $\vec{E} = E_0 e^{(i\omega t - \vec{k}\cdot r)}\hat{\mathrm{e}}$, we obtain for the coherence, in stationary regime (the resolution of this problem can be found in (BOYD et al., 1981)):

$$\sigma_{12} = \frac{-i(\rho_{11} - \rho_{22})\Omega_{12}}{i\delta_{12}^0 + \gamma_{12} + \gamma'}, \tag{2.6}$$

where ρ_{ii} are the populations, δ_{12}^0 is the frequency detuning, γ_{12} is the rate decay and γ' is related to the flight time. Ω_{12} is the Rabi's frequency:

$$\Omega_{12} = \frac{\mu_{12} E_0}{\hbar}.$$

Due to the Doppler effect we have that the frequency detuning will depend on the velocity

Figure 4 – The variation of the refractive index concerning light frequency detuning Δ is depicted both in the absence (n) and presence $(n\pm)$ of a magnetic field. The illustration corresponds to the scenario where $2g\mu B = \hbar\Gamma$.

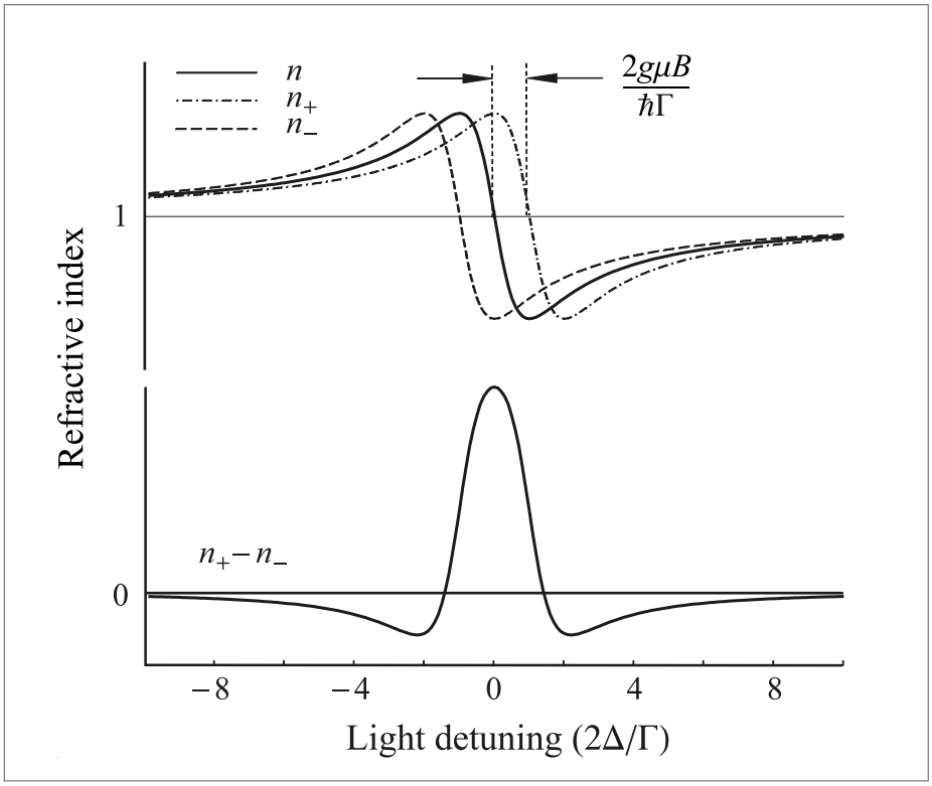

Source: taken from referencec (BUDKER et al., 2002)

of the atoms. Thus, we need to integrate in velocity:

$$\delta_{12}^{0} = \delta_{12} + \omega_b \frac{v}{c},$$

where ω_b is the frequency of the beam b, v is the velocity of the atom and c is the velocity of the light. Considering $\rho_{11} \approx 1$, we can write:

$$\chi_{ij} = \frac{2N\mu_{ij}^2}{\epsilon_0 \hbar} R_i, \tag{2.7}$$

where R_i is given by:

$$R_i = \int_{-\infty}^{\infty} \frac{1}{\gamma_{12} - i\left(\delta_{12} + \omega_b \frac{v}{c}\right)} f(v)\, dv,$$

and $f(v)$ is the velocity distribution assumed to obey the Maxwell-Boltzmann distribution as: (MüLLER-KIRSTEN, 2022)

$$f(v)dv = \frac{1}{u\sqrt{\pi}} \int e^{\frac{-v^2}{u^2}} dv, \tag{2.8}$$

where u is the most probable velocity in the ensemble:

$$u = \frac{2k_B T}{m}, \tag{2.9}$$

k_b is the Boltzmann constant and m is the mass of the particle. Considering the magnetic dipole interaction, the frequency detuning will be given by:

$$\delta_{12}^{0} = \delta_{12} + \omega_b \frac{v}{c} + \frac{\mu_b}{\hbar} g_F m_F B_z.$$

We will have to sum over all hyperfine sublevels, for the σ^+ and σ^- transitions, illustrated in figures 5 and 6. As we can see in the figures, there are many transitions and because of that we also need to take into account the electric dipole moment of each transition and the shift of each sublevel so the calculation of the rotation angle is not simple.

In fact, we will not calculate the Faraday rotation angle, but rather measure this angle and then compare it with existing values in the literature.

Figure 5 – All σ^+ and σ^- transitions from F = 2 to F' = 1,2,3. There is a total of 24 transitions. The green lines show the σ^+ transitions and the pink lines the σ^- transitions.

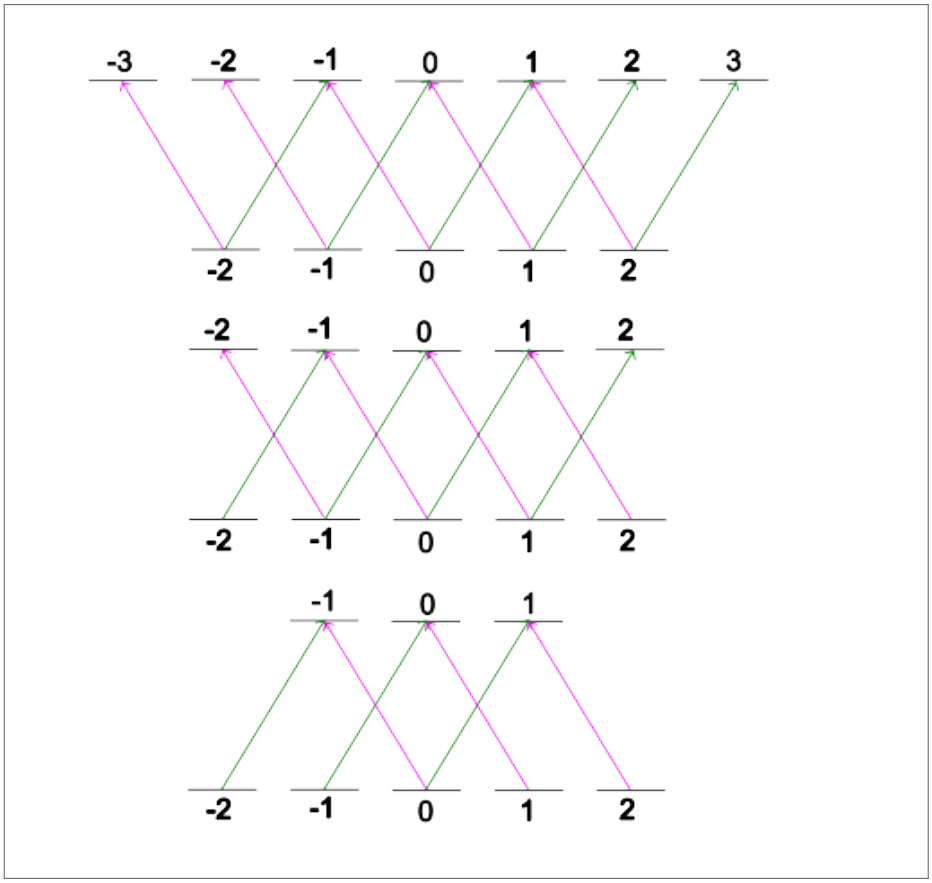

Source: the author (2024)

Figure 6 – All σ^+ and σ^- transitions from $F_g = 3$ to $F' = 2, 3, 4$. There is a total of 36 transitions. The green lines show the σ^+ transitions and the pink lines the σ^- transitions.

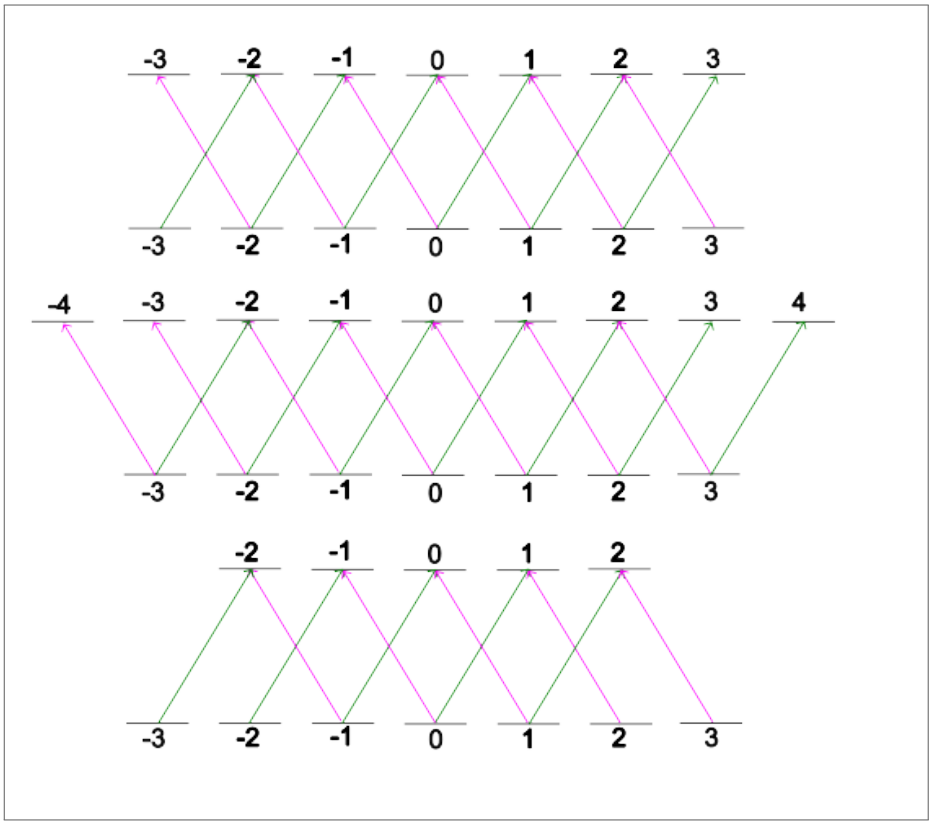

Source: the author (2024)

2.1 THE FARADAY EFFECT EXPERIMENT

For our experiments, we used a saturation absorption spectroscopy as a rule to measure the laser frequency. In this section, we are going to explain the experimental setup for the Faraday effect, as well as the saturated absorption spectroscopy.

2.1.1 Saturated Absorption Spectroscopy

In figure 7 we have a linear absorption spectrum for rubidium atoms in a cell. We see four dips, each one corresponds to a transition from one hyperfine level from the ground state $5S_{1/2}$ to the excited state $5P_{3/2}$ of rubidium, as indicated. The dips have a Gaussian-like format and hide the hyperfine structure of the excited state due to Doppler broadening. Saturated absorption spectroscopy is a powerful way to eliminate this effect and allows us to measure the hyperfine energy levels of the sample.

Figure 7 – Linear absorption spectroscopy of rubidium D_2 line. With this method we cannot see the hyperfine transitions.

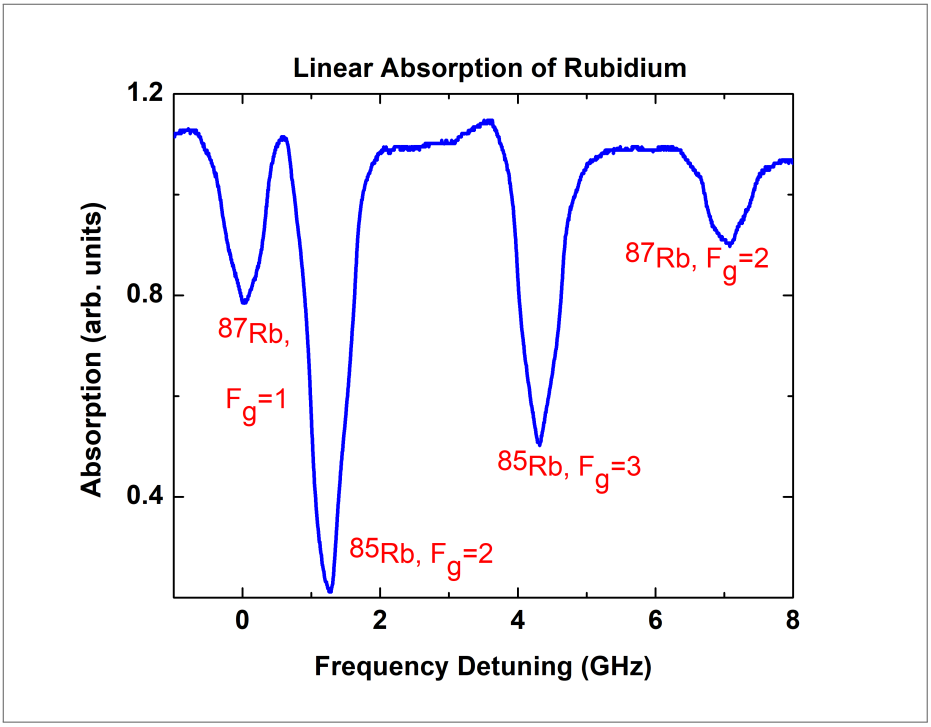

Source: the author (2023)

In the linear absorption spectroscopy, when we pass the laser beam through the vapour cell, with a frequency ω_L in the laboratory reference frame, each atom has a random velocity and then each one of them sees the laser with a different Doppler frequency, ω, related to

their velocities in the z direction, v_z, through the equation:

$$\omega = \omega_L \left[1 - \frac{v_z}{c}\right], \tag{2.10}$$

where c is the velocity of light and $v_z << c$.

Because the atoms have different velocities they absorb energy at different frequencies, obeying the Maxwell-Boltzmann distribution and thus the peaks are gaussians, with a width at half height of the order of 500 MHz. The excited states are only 29 to 270 MHz apart and cannot be seen using this simpler spectroscopy technique.

Figure 8 – Saturated absorption spectroscopy experimental setup

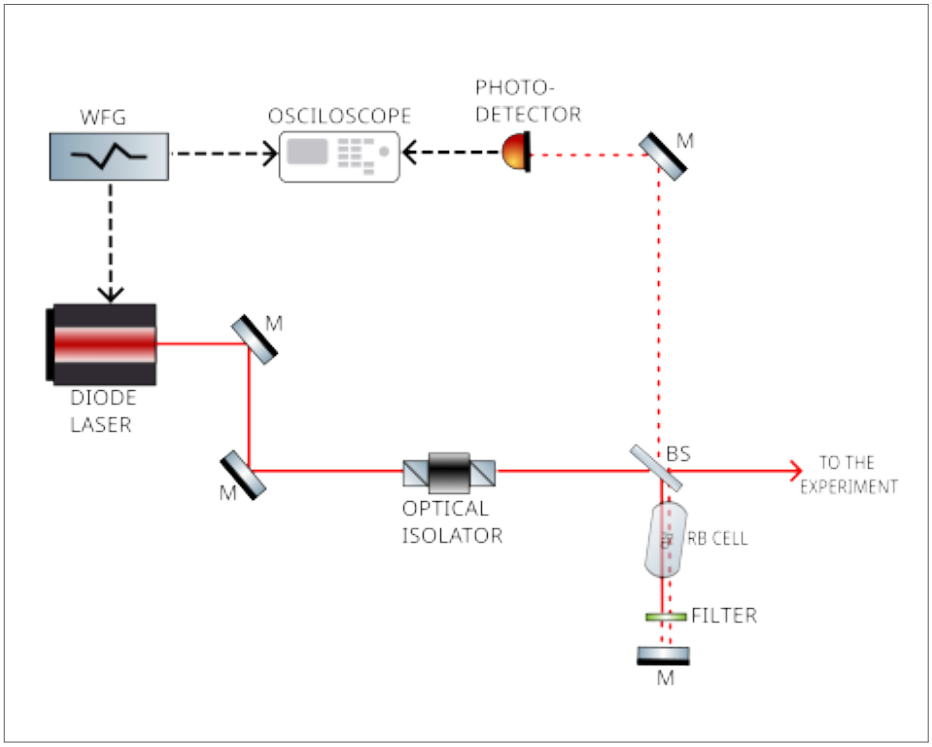

Source: the author (2024)

Saturated absorption spectroscopy allows observation of hyperfine excited states hidden by Doppler broadening. The experimental scheme is very simple and can be seen in figure 8. For the saturation absorption spectroscopy we use a diode laser from Sanyo, model DL7140-201S, with $\lambda = 780$ nm, with homemade electronics for current and temperature control. We modulate the frequency of the laser using a wave form generator (WFG) from Agilent, model 33521A. This laser will also be used in the main experiments, the Faraday's rotation and the four wave mixing. We first pass the beam through an optical isolator to avoid reflected light from returning to the laser head. Then, the laser beam passes through a non polarizing beam splitter (a simple thin glass plate), letting only a small part of the laser beam (about 10 %)

pass through the rubidium cell (JACQUES et al., 2009). We place a neutral density (ND) filter after the cell to obtain a much smaller intensity beam and reflect it back to the cell in such a way that we have two counter propagating beams, one much more intense than the other crossing in the middle of the cell. Since the beams are counter propagating, each one of them interacts with a different velocity group except for the atoms with $v_z = 0$. In this situation the pump beam saturates the transitions, causing a decrease in the absorption of the probe beam, and thus showing us peaks in the Doppler profiles, as seen in figure 9.

Figure 9 – Saturated absorption spectroscopy of rubidium. With this technique we can see the hyperfine levels inside the Doppler profile.

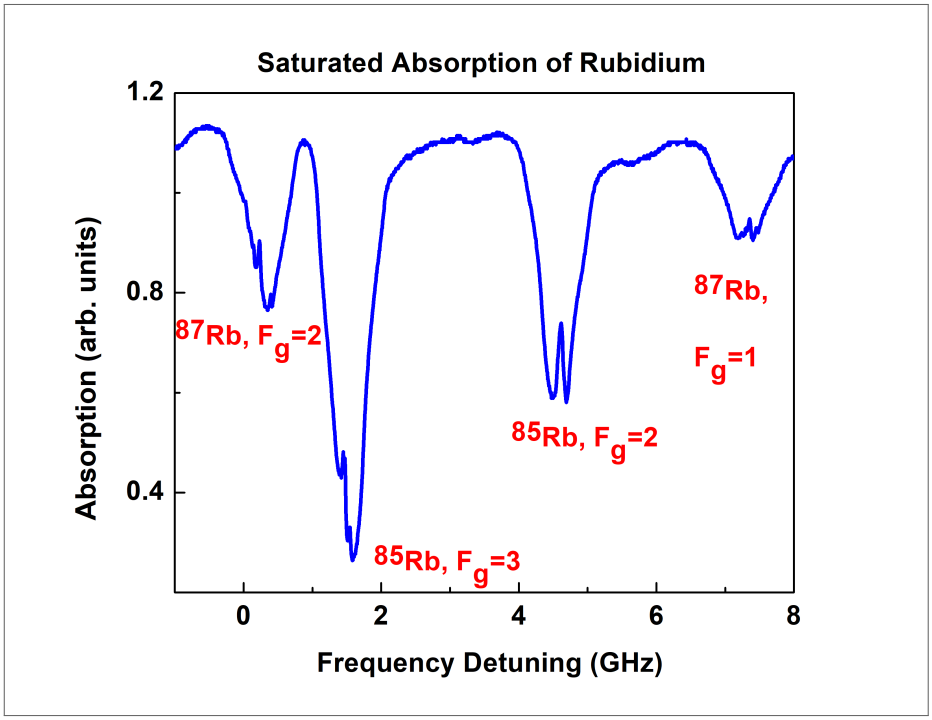

Source: the author (2024)

We could expect three peaks in each profile, since the quantum number F obeys the selection rule: $\Delta F = 0, \pm 1$, each peak corresponding to one of the three possible transitions from the ground hyperfine state to an excited state. We see, however, six peaks, three due to the pure transitions and three due to the crossover transitions, as shown in figure 10. The crossover peaks occur when two transitions are very close to each other, in such a way that the difference between them is smaller than the Doppler broadening and the laser frequency is exactly in the middle point between the two pure transitions. In this situation both beams interact with the same velocity group $\pm v$, but each one of them interacts with a different pure transition. The pump beam saturates the transition, and we see a decrease in the absorption of the probe beam, generating an extra peak in the Doppler profile.

Figure 10 – Saturated absorption spectroscopy of rubidium. We can see the three hyperfine transitions and the crossover transitions, as indicated.

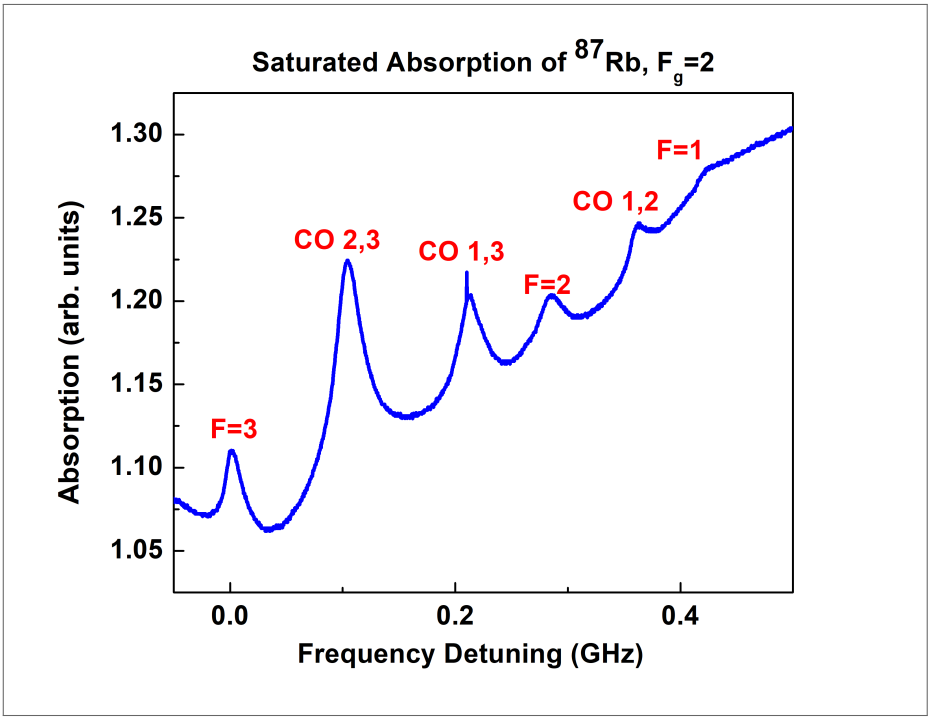

Source: the author (2024)

2.1.2 Faraday Rotation

The experimental setup for the Faraday rotation is shown in figure 11. We use saturated absorption spectroscopy to monitor the laser frequency. The transmitted part of the laser beam divided in the SAS experiment will be used for the Faraday's rotation experiment (about 90 % of the laser power). The laser beam goes through an optical fiber to have a spatially well-defined profile. We then pass the laser through another optical isolator to eliminate any reflections in the laser head due to the optical fiber. With a polarizing beam splitter (PBS) we divide the beam in two, with linear perpendicular polarizations and the power of each side is controlled using a half wave plate before the PBS. We use guide masks to align the laser beams in such a way that there is a small angle between them and that they cross each other in the center of the rubidium vapor cell, like in figure 12. To confirm that the effect we were seeing was caused by a the interaction of the atoms with an external magnetic field, we used a magnetic shield, a metallic cylinder with a hole for the light beam to pass through. Figure 13 shows the same experimental setup for the Faraday's rotation, but with the magnetic shield positioned. In this case, with the magnetic shield, no rotation is observed, since the shield blocks the external magnetic field. After passing the cell, each beam follows its direction. To

detect the Faraday rotation, we measure the intensity of the beam that is transmitted with polarization perpendicular to the incident polarization. We use a half wave plate between the cell and the third PBS to align the detector and then remove the plate. The external magnetic field under which the sample is subjected is the Earth's magnetic field, with magnitude of 0.5 G, which goes near zero when we use the magnetic shield. To measure the Earth magnetic field strength and its direction we used a gaussimeter which we borrowed from the magnetism lab. We measured a field of an order of 0.5 G and in about the same direction of the beam passing through the cell. Our results indicate that the Earth's magnetic field is responsible for the observed Faraday effect. We use two beams because we are also interested in studying the FWM process, where the nonlinear signal is generated when atoms interact simultaneously with two beams. We will call the beam that is being transmitted by PBS 1 beam a and the beam that is reflected by PBS 1 as beam b, as depicted in figures 11 and 13. Beams a and b have the same diameter. For most experiments, with higher intensity, we used a beam diameter of 0.32 mm.

Figure 11 – Faraday's rotation experimental setup

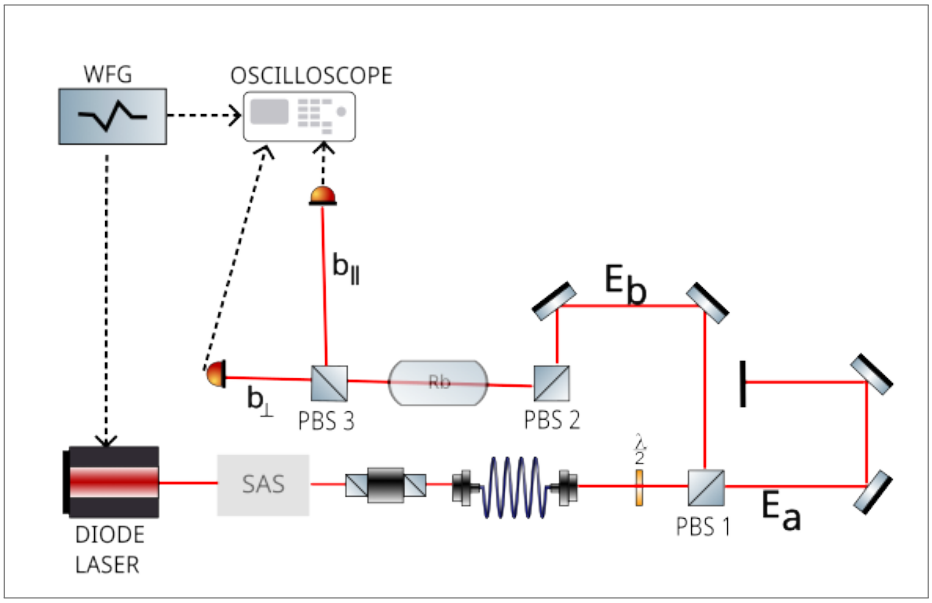

Source: the author (2024)

For the Faraday rotation we have done experiments for different situations: (i) varying the b beam intensity, to see the influence of intensity in the rotation peaks; (ii) varying the temperature, to check how the rotation varies with atomic density; (iii) with and without a magnetic shield, to verify that the effect of polarization rotation that we were seeing was, in fact, the Faraday effect and (iv) with different intensities of beam a to see if there is an

Figure 12 – We pass the beams a and b through guide mask in such a way that there is a small angle between them and they cross in the center of the cell

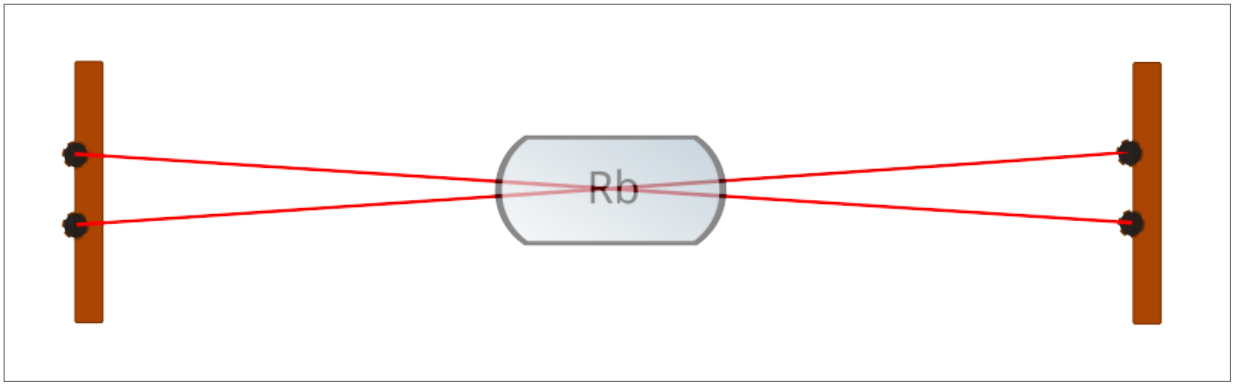

Source: the author (2024)

Figure 13 – Faraday's rotation experimental setup: we used a magnetic shield to check that the effect was due to an external magnetic field.

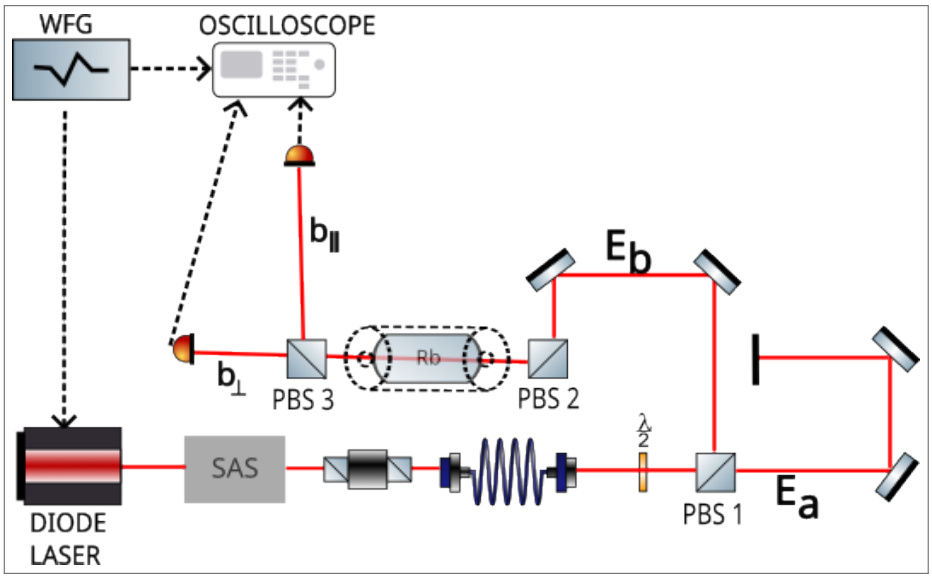

Source: the author (2024)

influence of a second beam in Faraday's rotation.

2.2 RESULTS

In figure 14 we see two curves of the intensity of the perpendicular component of beam b: one obtained without of a magnetic shield (green curve) and another one using the magnetic shield (pink curve). For these measurements we blocked beam a. Because the polarizers we have used are not perfect a small part of the light goes through the wrong direction, and we see in the pink curve an absorption of this light. In the green curve, we have the rotation of polarization by the Faraday effect. The two peaks indicated that the rotation occurs at the resonance, for the two isotopes.

Figure 14 – The intensity of the perpendicular component of beam b as a function of the laser detuning, with and without a magnetic shield. $I_b = 370$ mW/cm^2

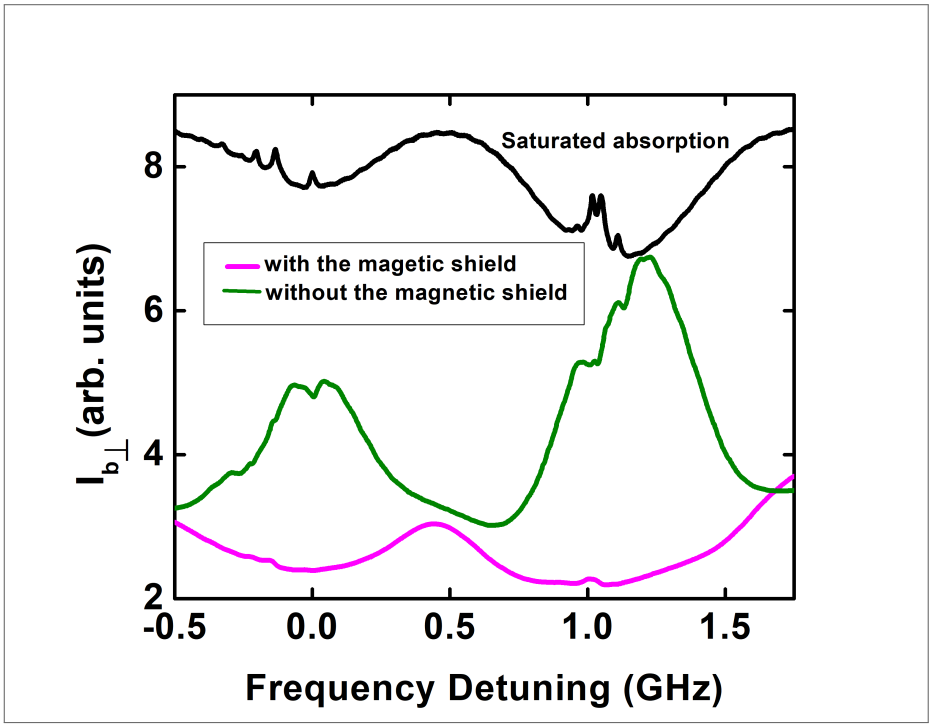

Source: the author (2024)

Figure 15 shows the intensity of the perpendicular component of beam b for different input intensities as a function of the frequency detuning. The black curve is the saturated absorption. For these measurements, the beam a is blocked. The pink curve is for a higher intensity: 890 mW/cm^2. We see the polarization rotation peaks only for the $^{87}Rb, F_g = 2$ and the $^{85}Rb, F_g = 3$ transitions. Decreasing the incident beam intensity we start to see peaks in the other two Doppler profiles. For the green and blue curves a very small peak appear for the $^{87}Rb, F_g = 1$ and for the $^{85}Rb, F_g = 2$, while for the purple curve, when the intensity is set to

Figure 15 – Intensity of the perpendicular component of beam b as a function of the laser detuning for different intensities of the incident beam.

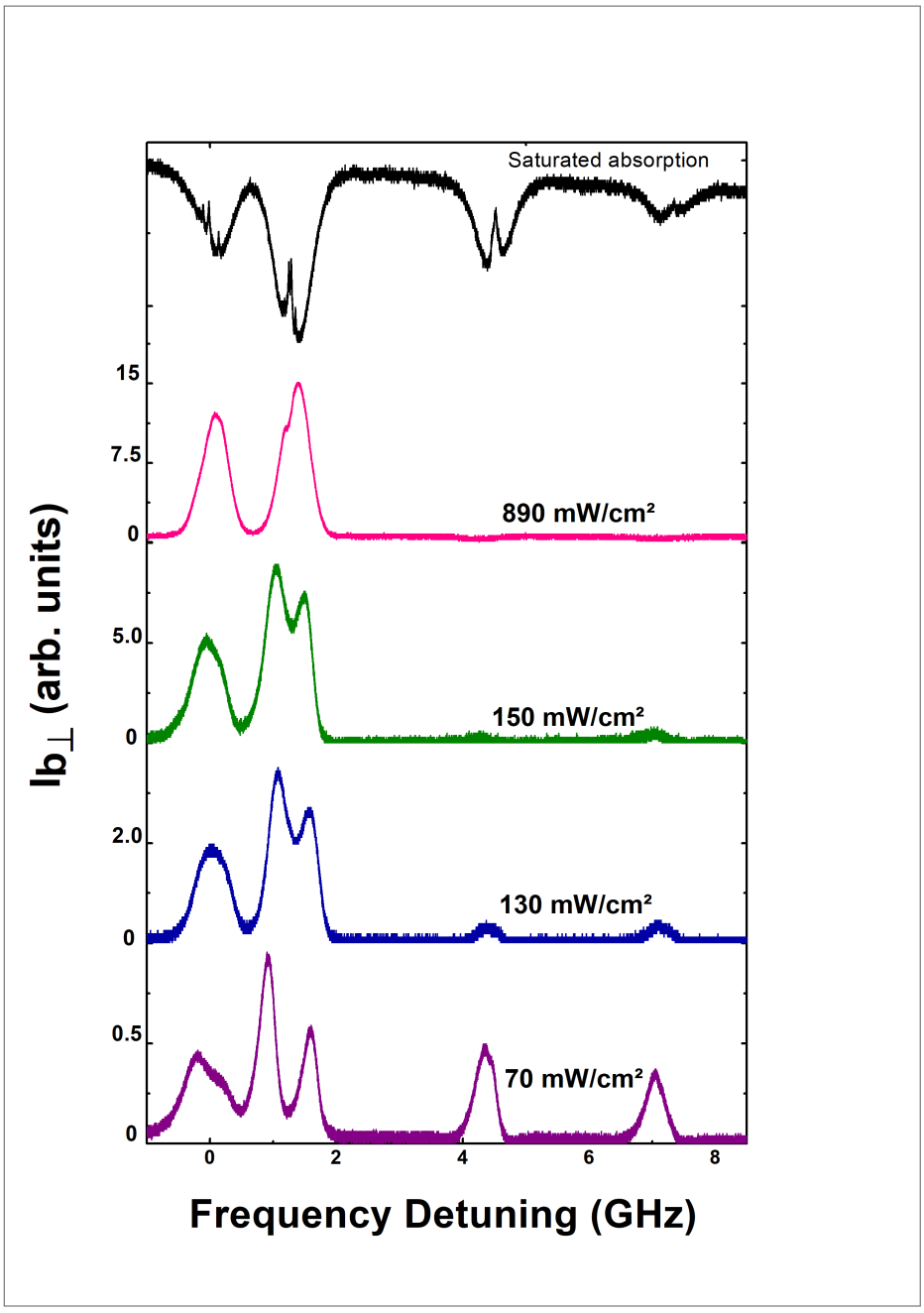

Source: the author (2024)

be 70 mW/cm^2, a clear rotation of polarization is observed for the four Dopplers of rubidium, where all the intensities were measured at the entrance of the cell. We understand that the reason for the observed polarization rotation only for two Dopplers, when the incident beam intensity is very high, is associated with an optical pumping process.

The process of optical pumping can be exemplified as follows: for the ^{87}Rb the atoms are initially distributed in the $F_g = 1$ and $F_g = 2$ ground states. When the laser beam passes

through the sample the atoms go to the excited states. Our laser beam is varying in frequency so it passes through the resonances of all of the hyperfine transitions of the D_2 line. The transitions obey the selection rule $\Delta F = 0, \pm 1$. The atoms that are in the $F_g = 1$ state can be excited to the $F_e = 0, 1, 2$ states. Similarly, the atoms which are in the $F_g = 2$ state can be excited to the $F_e = 1, 2, 3$ states. There are two closed transitions, one for each ground state which is when the atom cannot decay to another ground state but its original one. The closed transitions are $F_g = 1 \rightarrow F_e = 0$ and the $F_g = 2 \rightarrow F_e = 3$ transitions. Because the frequency separation between the $F_e = 0, 1, 2$ are quite small, when we have a high intensity light passing by, the probability of the other transitions occur increase significantly and the atoms that are in the closed transition $F_g = 1 \rightarrow F_e = 0$ also decay to the $F_g = 2$ state. These atoms, which are now in the $F_g = 2$ state, can do the closed transition $F_g = 2 \rightarrow F_e = 3$ which is far in frequency from the $F_e = 0, 1, 2$ (see figure 2) resulting in the rapid depopulation of $F_g = 1$ state. This is the process of optical pumping: in this case, the atoms are pumped from the $F_g = 1$ to the $F_g = 2$ state (ŠKOLNIK; VUJIčIć; BAN, 2009).

We understand that the optical pumping process is responsible for the absence of the $^{87}Rb, F_g = 1$ and $^{85}Rb, F_g = 2$ Dopplers in the polarization rotation for higher intensities. The same process explained for the ^{87}Rb occurs for the ^{85}Rb, where the atoms are pumped from the $F_g = 2$ to the $F_g = 3$ state.

In figure 15 we also note that in the ^{85}Rb, $F_g = 3$ there is a dip in the Faraday rotation signal. We expect that this peak may be caused by the Stark effect, however, this is not very clear since the peak diminishes when the intensity increases. We did not investigate this effect because this is not our main interest in this work.

In figure 16 we see the results of the Faraday's rotation for different temperatures.The black curve corresponds to the saturated absorption. The other curves correspond to the intensity of the perpendicular part of beam b. For this high intensity, $I = 2.26$ W/cm^2, we see only the two peaks corresponding to the $^{87}Rb, F_g = 2$ and the $^{85}Rb, F_g = 3$ Doppler profiles. Because we worked mostly with intense beams we decided to focus in the $^{87}Rb, F_g = 2$ and the $^{85}Rb, F_g = 3$ Doppler profiles, where the rotation peaks appear even for higher intensities. It is very clear that the intensity $I_{b_\perp}$ increases with temperature and thus with atomic density.

To estimate the angle of rotation we need to measure the intensity of the two polarization components of the incident beam. We can understand this remembering that we measure

Figure 16 – Intensity of the perpendicular component of the incident beam b as a function of the frequency detuning of beam b at different temperatures.

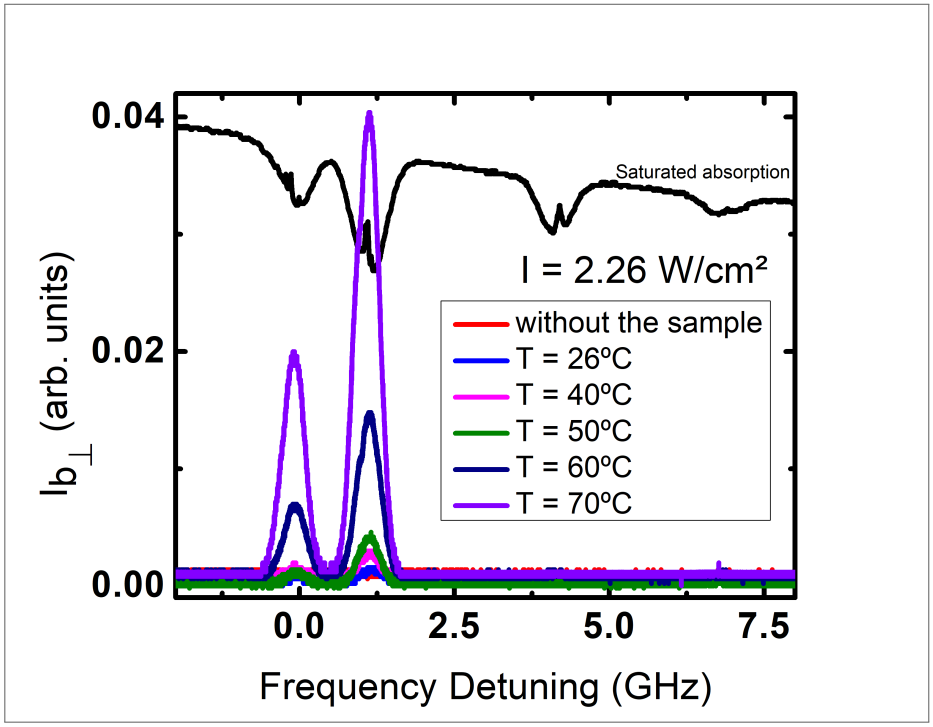

Source: the author (2024)

intensity:

$$\phi = \frac{1}{2} cos^{-1}\left(\frac{I_{b_\perp} - I_{b_\parallel}}{I_{b_\perp} + I_{b_\parallel}}\right), \tag{2.11}$$

where $I_{b_\perp}$ is the intensity of the perpendicular component of beam b, transmitted by PBS 3, $I_{b_\parallel}$ is the intensity of the parallel component of beam b, reflected by PBS 3. This formula can be used because the intensity of each side (parallel or perpendicular) is a component of the squared vector of the electric field:

$$I_{b_\perp} = I sin^2\phi \tag{2.12}$$

$$I_{b_\parallel} = I cos^2\phi \tag{2.13}$$

then

$$I_{b_\perp} - I_{b_\parallel} = I(sen^2\phi - cos^2\phi) = I cos(2\phi) \tag{2.14}$$

since

$$I = I_{b_\perp} + I_{b_\parallel} \tag{2.15}$$

is the total intensity of beam b we have that:

$$cos(2\phi) = \frac{I_{b_\perp} - I_{b_\parallel}}{I_{b_\perp} + I_{b_\parallel}}, \tag{2.16}$$

and thus

$$\phi = \frac{1}{2} cos^{-1}\left(\frac{I_{b_\perp} - I_{b_\parallel}}{I_{b_\perp} + I_{b_\parallel}}\right). \tag{2.17}$$

For using this formula we had to mesure $I_{b_\perp}$ and $I_{b_\parallel}$ simultaneously. In figure 17 we show the intensity difference,$I_{b_\perp} - I_{b_\parallel}$, between the two polarizations, normalized by the total intensity, $I_{b_\perp} + I_{b_\parallel}$, as function of the frequency detuning. From this figure, we can see that the rotation angle reaches its maximum at the resonances, where $\frac{I_{b_\perp} - I_{b_\parallel}}{I_{b_\perp} + I_{b_\parallel}}$ is minimum. We

Figure 17 – Intensity difference between the two polarizations, normalized by the total intensity, as a function of the frequency detuning

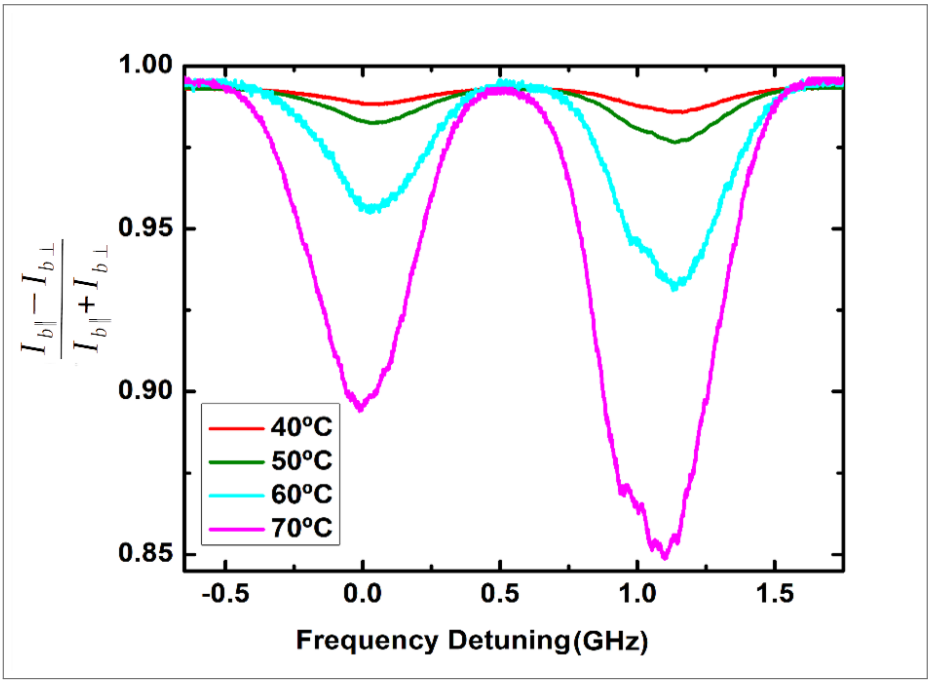

Source: the author (2024)

took the minimum points of figure 17 to calculate the angles shown in figure 18. For the 70ºC curve, corresponding to an atomic density of $7.31 \times 10^{12} at/cm^3$, in the ^{85}Rb minimum we have $\frac{I_{b_\perp} - I_{b_\parallel}}{I_{b_\perp} + I_{b_\parallel}} = 0.85$. This give a rotation angle of:

$$\phi = \frac{1}{2} cos^{-1}(0.85) = 0.28° = 4.9 \pm 0.2 \text{ mrad}. \tag{2.18}$$

On literature we find a Verdet constant $V = 1.4 \times 10^3$ rad T^{-1} m^{-1} (WELLER et al., 2012). For the geomagnetic field of 0.5 G and the cell length of 5 cm it predicts an angle of 3.5 mrad, in the same order of magnitude of our result.

In figures 18 and 19 we see the dependence of the rotation angle with the atomic density. For calculating the atomic densities from the temperature we used (GLORIEUX et al., 2023):

$$n = \frac{10^{9,318-\frac{4040}{T}}}{k_B T}, \tag{2.19}$$

where T is the sample temperature in Kelvin and k_B is Boltzmann constant. We made then a linear fit, we can verify if the Verdet constant we have got from our data matches with the one on literature.

Figure 18 – Rotation angle vs the atomic density for ^{85}Rb. The red line is the linear fit

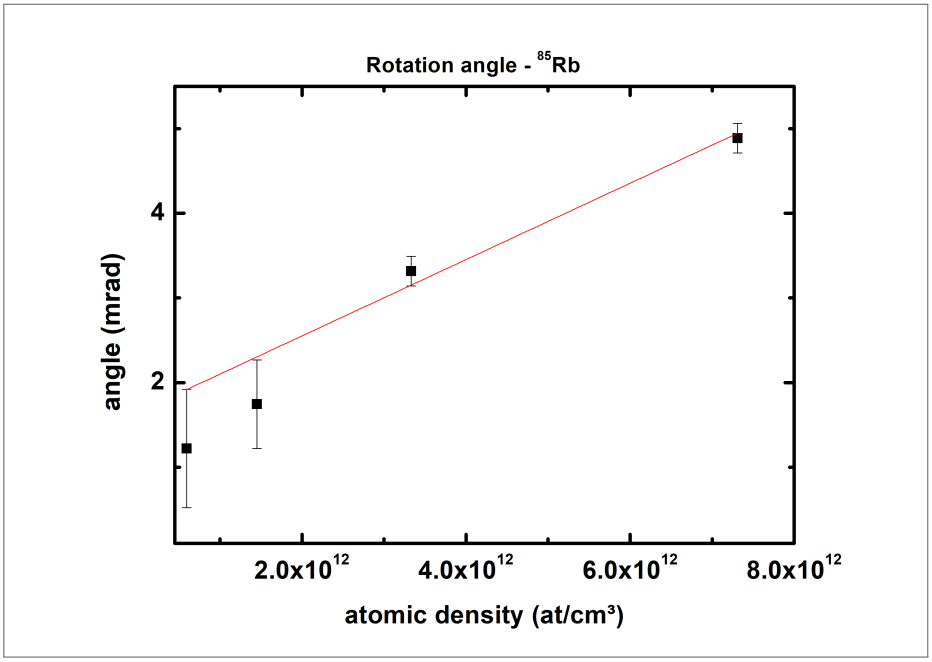

Source: the author (2024)

To verify the Verdet constant we used equation 2.1:

$$\phi = VBL$$

Because the atomic density is not explicitly given in this formula we divide and multiply the right hand side by ΔN:

$$\phi = VBL\frac{\Delta N}{\Delta N} \tag{2.20}$$

The angular coefficient α of the linear fit given by the plot of the angle versus the atomic density. We can write:

$$\alpha = \frac{\Delta\phi}{\Delta N} = \frac{VBL}{\Delta N},$$

Figure 19 – Rotation angle vs the atomic density for ^{87}Rb. The red line is the linear fit

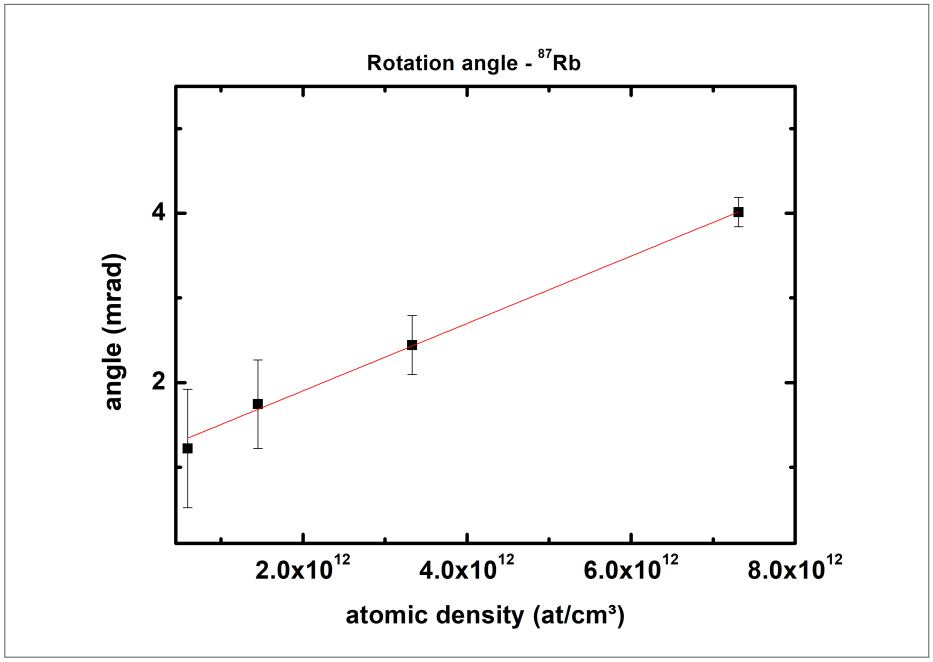

.

Source: the author (2024)

and

$$\frac{\alpha}{BL} = \frac{V}{\Delta N}$$

so

$$V = \frac{\alpha}{BL}\Delta N$$

The angular coefficient of the ^{87}Rb rotation angle linear fit is about $\alpha = 4 \times 10^{-13} \frac{\text{mrad}}{\text{cm}}$. Using the geomagnetic field $B = 0.5$ G, and knowing that the length of the cell is $L = 5$ cm, we obtain:

$$\frac{V}{\Delta N} = \frac{4 \times 10^{-13}}{0.5 \times 5} \frac{\text{mrad} \times \text{cm}^2}{\text{at} \times \text{G}} = 1.6 \times 10^{-16} \frac{\text{rad} \times \text{cm}^2}{\text{at} \times \text{G}}.$$

The atomic density interval we are working on is $\Delta N = 7 \times 10^{12}$, as seen in figure 18 and we find:

$$V = 1.6 \times 10^{-16} \times 7 \times 10^{12} = 11 \times 10^{-4} \frac{\text{rad}}{\text{G} \times \text{cm}} = 1.1 \times 10^{3} \frac{\text{rad}}{\text{T} \times \text{m}}. \tag{2.21}$$

As said before, the Verdet constant we found on literature is 1.4×10^3 rad $\text{T}^{-1}\text{m}^{-1}$ (WELLER et al., 2012), showing us that our result is reasonable. In fact, the values of the rotation angle and the Verdet constant clearly indicate that what we are observing is a Faraday rotation, in a linear regime related to the external magnetic field.

Figure 20 – Intensity of the perpendicular component of beam b in the presence of beam a for different intensities. $I_b = 500$ mW/cm^2

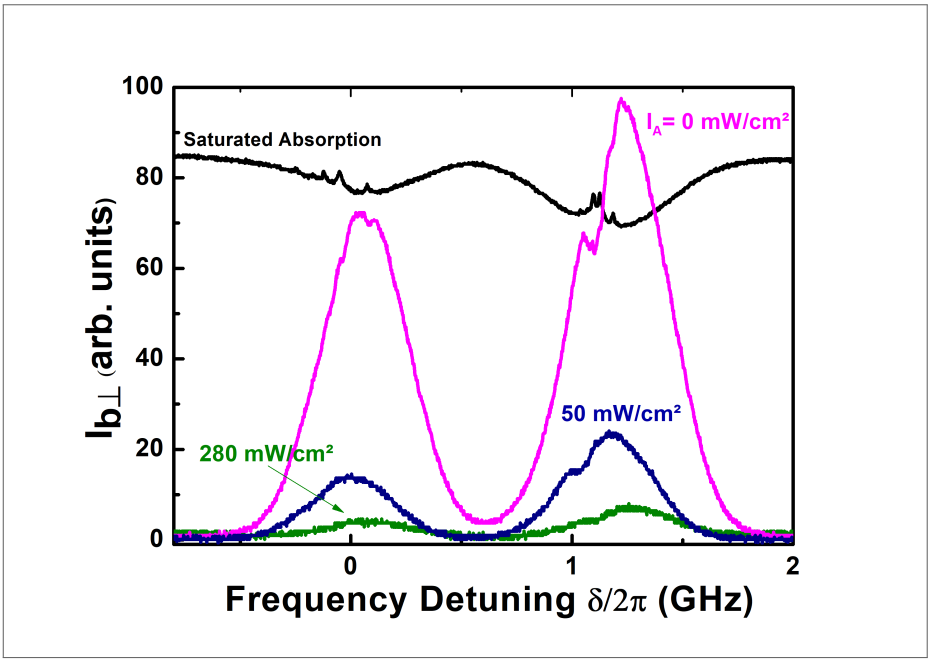

Source: the author (2024)

In figure 20 we investigated the effect of a second beam in the sample. The green curve is the Faraday polarization rotation without the presence of a second beam. The pink and blue curves show the Faraday rotation in the presence of a second beam. We can see that the polarization rotation decreases.

In the literature, we find that a second beam is frequently used to control the Faraday polarization rotation, for example, in (PATNAIK; AGARWAL, 2001) a second beam with circular polarization is used to enhance the Faraday rotation. In our case, we observe a decrease in the signal. This may occur because both laser beams are varying in frequency simultaneously and as a result, when one laser beam is in resonance, so is the other. Consequently, both beams interact with the same group of atoms at the same time and can then inhibit each other's rotation process.

3 FOUR WAVE MIXING

In this chapter we are going to focus in the four wave mixing experiment. First, we give a brief introduction to the four wave mixing process, followed by a simple theoretical overview of a three-level system, then we explain the experimental setup, and lastly we show our results.

3.1 NON-LINEAR OPTICS - FOUR WAVE MIXING

The optical response of a non-linear medium due to the interaction with electromagnetic fields can be described through the polarization induced in the medium, which represents the dipole moment per unit volume. The polarization $\vec{P}$ can be expressed as a power series in terms of the electric field $\vec{E}$ (BOYD, 2008):

$$\vec{P} = \varepsilon_0 \left(\chi^{(1)} E + \chi^{(2)} E^2 + \chi^{(3)} E^3 \right), \tag{3.1}$$

where χ^n is the nth order optical susceptibility of the medium. Because atomic vapors are centrosymetric systems, the first non-linear term is the third order one, given by $\chi^{(3)}$.

When two incident fields of frequencies ω_a and ω_b interact with a medium characterized by a thrid order susceptibility, $\chi^{(3)}$, various frequency combinations are allowed. In this work, we are particularly interested in the $2\omega_b - \omega_a$ combination, that is, in the four wave mixing (FWM) process where two photons of beam b are absorbed and one photon of beam a is emitted, generating a new field. Figure 21 shows the two fields E_a and E_b interacting with a non-linear medium in such a way that two four wave mixing signals are emitted. There is conservation of momentum and energy in such a way that we can predict the energy and direction of each FWM signal. Figure 22 shows the spatial orientation of the wave-vectors of the incident and generated beams involved in the FWM process, with a schematic representation of phase-matching.

The associated polarization is given by (BOYD, 2008):

$$P(2\omega_b - \omega_a) = 3\varepsilon_0 \chi^{(3)} E_b^2 E_a^*, \tag{3.2}$$

where the factor of 3 accounts for different field permutations contributing to this polarization term. $\chi^{(3)}$ is the third order nonlinear susceptibility that contain the information about the

Figure 21 – The directions of input and output beams of the FWM near interaction region.

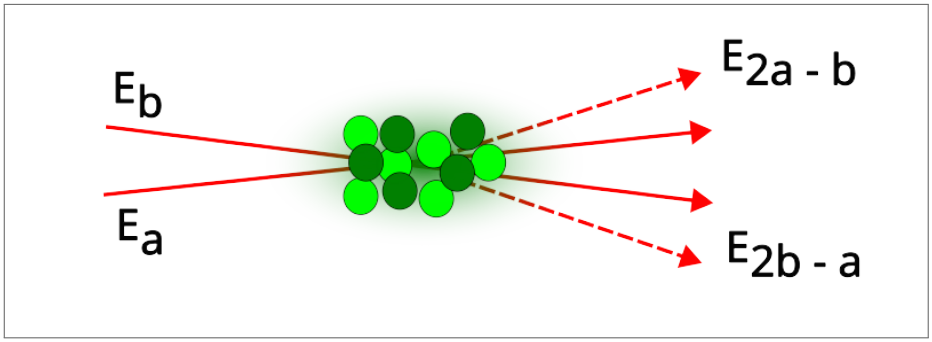

Source: the author (2024)

Figure 22 – The spatial orientation of the wave-vectors of both the incident and generated beams of the four wave mixing process.

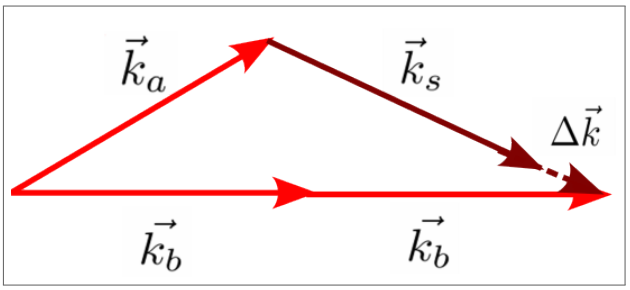

Source: the author (2024)

interaction of the driven fields and the atomic medium. This nonlinear susceptibility can be calculated using the density matrix formalism with a semiclassical treatment, considering the electromagnetic fields as classical quantities and quantitizing the atomic medium. A very simple treatment for our system is presented in the following section.

3.1.1 The three level system for the four wave mixing

For a theoretical description of the FWM signal,we can use a three level system with two fields, E_a and E_b, interacting with the atomic medium, as shown in figure 23. In the case of the FWM signal that we are investigating it is important to take into account that in the experiment we have two beams with the same frequency and that they have orthogonal linear polarizations. The Hamiltonian of such a scheme can be written as the free atom one plus the interaction Hamiltonian, which we will consider as an electric dipole interaction. The matrix

representing the Hamiltonian is then:

$$\begin{pmatrix} H_1 & H_{int_{12}} & 0 \\ H_{int_{21}} & H_2 & H_{int_{23}} \\ 0 & H_{int_{32}} & H_3 \end{pmatrix} \tag{3.3}$$

where $H_{int} = -\vec{\mu} \cdot \vec{E}$. We are not considering any interaction between the ground states $|1\rangle$ and $|3\rangle$, the components of the Hamiltonian matrix H_{13} and H_{31} are both equal to zero.

Figure 23 – Three level scheme for two fields.

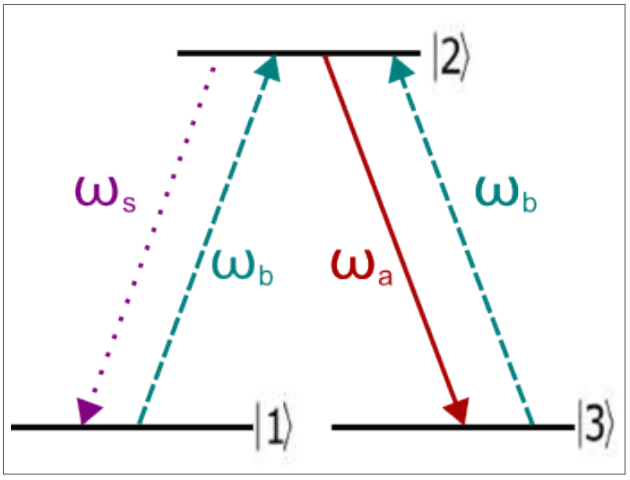

Source: the author (2024)

The electric fields can be written as:

$$\vec{E_\alpha} = \varepsilon_\alpha e^{-i(\vec{k_\alpha}\cdot\vec{r}-\omega_\alpha t)}\ \hat{e_\alpha},\ \ \alpha = a, b. \tag{3.4}$$

From the electric field we can write the Rabi's frequencies:

$$\Omega_{ij} = \frac{\mu_{ij}\varepsilon_\alpha}{\hbar}. \tag{3.5}$$

To resolve this problem we can use the density matrix formalism. The Liouville equation relates the density matrix to the Hamiltonian:

$$\dot{\rho} = \frac{i}{\hbar}[\hat{\rho}, \hat{H}]. \tag{3.6}$$

We can use the completeness relations to obtain the equations for populations and coherences:

$$\dot{\rho_{ij}} = \frac{i}{\hbar}\sum_l (\rho_{il}H_{lj} - H_{il}\rho_{lj}), \tag{3.7}$$

so:

$$\dot{\rho_{11}} = \frac{i}{\hbar}\left(\rho_{11}H_{11} + \rho_{12}H_{21} + \rho_{13}H_{31} - H_{11}\rho_{11} - \rho_{21}H_{12} - \rho_{31}H_{13}\right), \tag{3.8}$$

$$\dot{\rho_{22}} = \frac{i}{\hbar}\left(\rho_{21}H_{12} + \rho_{22}H_{22} + \rho_{23}H_{32} - \rho_{12}H_{21} - \rho_{22}H_{22} - \rho_{32}H_{23}\right), \tag{3.9}$$

$$\dot{\rho_{33}} = \frac{i}{\hbar}\left(\rho_{31}H_{13} + \rho_{32}H_{23} + \rho_{33}H_{33} - \rho_{13}H_{31} - \rho_{23}H_{32} - \rho_{33}H_{33}\right), \tag{3.10}$$

$$\dot{\rho_{12}} = \frac{i}{\hbar}\left[(\rho_{11} - \rho_{22})H_{12} + (E_2 - E_1)\rho_{12} + \rho_{13}H_{32} - \rho_{32}H_{13}\right], \tag{3.11}$$

$$\dot{\rho_{13}} = \frac{i}{\hbar}\left[(E_3 - E_1)\rho_{13} + \rho_{11}H_{13} + \rho_{12}H_{23} - \rho_{23}H_{12} - \rho_{33}H_{13}\right], \tag{3.12}$$

$$\dot{\rho_{32}} = \frac{i}{\hbar}\left[(\rho_{33} - \rho_{22})H_{32} + (E_2 - E_3)\rho_{32} + \rho_{12}H_{31} + \rho_{31}H_{12}\right], \tag{3.13}$$

where E_1, E_2, E_3 are the energy of each level. Simplifying and substituting the Hamiltonian components $H_{int_{ij}} = -\hbar\Omega_{ij}e^{-i(\vec{k_\alpha}\cdot\vec{r}-\omega_\alpha t)}$:

$$\dot{\rho_{11}} = -i\left[\rho_{12}\Omega_{21}e^{i(\vec{k_a}\cdot\vec{r}-\omega_a t)} - \rho_{21}\Omega_{12}e^{-i(\vec{k_a}\cdot\vec{r}-\omega_a t)}\right], \tag{3.14}$$

$$\dot{\rho_{22}} = -i\left[\rho_{21}\Omega_{12}e^{-i(\vec{k_a}\cdot\vec{r}-\omega_a t)} + \rho_{23}\Omega_{32}e^{-i(\vec{k_b}\cdot\vec{r}-\omega_b t)} - \rho_{12}\Omega_{21}e^{i(\vec{k_a}\cdot\vec{r}-\omega_a t)} - \rho_{32}\Omega_{23}e^{i(\vec{k_b}\cdot\vec{r}-\omega_b t)}\right], \tag{3.15}$$

$$\dot{\rho_{33}} = -i\left[\rho_{32}\Omega_{23}e^{i(\vec{k_b}\cdot\vec{r}-\omega_b t)} - \rho_{23}\Omega_{32}e^{-i(\vec{k_b}\cdot\vec{r}-\omega_b t)}\right], \tag{3.16}$$

$$\dot{\rho_{12}} = -i\left[(\rho_{11} - \rho_{22})\Omega_{12}e^{-i(\vec{k_a}\cdot\vec{r}-\omega_a t)} + \frac{(E_2 - E_1)\rho_{12}}{\hbar} + \rho_{13}\Omega_{32}e^{-i(\vec{k_b}\cdot\vec{r}-\omega_b t)}\right] \tag{3.17}$$

$$\dot{\rho_{13}} = -i\left[\frac{(E_1 - E_3)\rho_{13}}{\hbar} + \rho_{12}\Omega_{23}e^{i(\vec{k_b}\cdot\vec{r}-\omega_b t)} - \rho_{23}\Omega_{12}e^{-i(\vec{k_a}\cdot\vec{r}-\omega_a t)}\right] \tag{3.18}$$

$$\dot{\rho_{32}} = -i\left[(\rho_{33} - \rho_{22})\Omega_{32}e^{-i(\vec{k_b}\cdot\vec{r}-\omega_b t)} - \frac{(E_2 - E_3)\rho_{32}}{\hbar} - \rho_{31}\Omega_{12}e^{-i(\vec{k_a}\cdot\vec{r}-\omega_a t)}\right] \tag{3.19}$$

At this point, we introduce the slow variables of the system to later eliminate explicit time dependence.

$$\rho_{12} = \sigma_{12}e^{i\omega_a t} \tag{3.20}$$

$$\rho_{32} = \sigma_{32}e^{i\omega_b t} \tag{3.21}$$

$$\rho_{13} = \sigma_{13}e^{i(\omega_a - \omega_b)t}, \tag{3.22}$$

We also consider a perfect phase-matching:

$$\Delta k = 2k_b - k_a - k_s = 0, \tag{3.23}$$

so we can rewrite the density matrix elements as (using $\Omega e^{i\vec{k}\cdot\vec{r}}$ as Ω to simplify notation):

$$\dot{\rho_{11}} = i(\sigma_{12}\Omega_{21} - \sigma_{21}\Omega_{12}) \tag{3.24}$$

$$\dot{\rho_{22}} = i(\sigma_{21}\Omega_{12} + \sigma_{23}\Omega_{32} - \sigma_{12}\Omega_{21} - \sigma_{32}\Omega_{23}) \tag{3.25}$$

$$\dot{\rho_{33}} = i(\sigma_{32}\Omega_{23} - \sigma_{23}\Omega_{32}) \tag{3.26}$$

$$\dot{\sigma}_{12} = i\left[(\rho_{22} - \rho_{11})\Omega_{12} + \frac{(E_1 - E_2)}{\hbar}\sigma_{12} - \sigma_{13}\Omega_{32} - i\omega_a\sigma_{12}\right] \tag{3.27}$$

$$\dot{\sigma}_{13} = i\left[-\sigma_{12}\Omega^*_{32} + \sigma_{13}\frac{(E_3 - E_1)}{\hbar} + \sigma^*_{23}\Omega^*_{12} - (\omega_a - \omega_b)\sigma_{13}\right] \tag{3.28}$$

$$\dot{\sigma}_{32} = i\left[(\rho_{22} - \rho_{33})\Omega_{32} + \frac{(E_2 - E_3)}{\hbar}\sigma_{32} - \sigma^*_{13}\Omega_{12} + i\omega_b\sigma_{32}\right] \tag{3.29}$$

Now, we can add the relaxation terms: γ', related to time of flight, γ_{ij}, related to the coherence and Γ_{ij}, related to the population:

$$\dot{\rho_{11}} = -i(\sigma_{12}\Omega_{21} - \sigma_{21}\Omega_{12}) - \gamma'(\rho_{11} - \rho^0_{11}) + \Gamma_{12}\rho_{22} \tag{3.30}$$

$$\dot{\rho_{22}} = -i(\sigma_{21}\Omega_{12} + \sigma_{23}\Omega_{32}e - \sigma_{12}\Omega_{21} - \sigma_{32}\Omega_{23}) - (\Gamma_{21} + \Gamma_{23} + \gamma')\rho_{22} \tag{3.31}$$

$$\dot{\rho_{33}} = -i(\sigma_{32}\Omega_{23} - \sigma_{23}\Omega_{32}) - \gamma'(\rho_{33} - \rho^0_{33}) + \Gamma_{23}\rho_{22} \tag{3.32}$$

$$\dot{\sigma}_{12} = i\left[(\rho_{22} - \rho_{11})\Omega_{12} + \frac{(E_1 - E_2)}{\hbar}\sigma_{12} - \sigma_{13}\Omega_{32} - i\omega_a\sigma_{12}\right] - (\gamma_{12} + \gamma')\sigma_{12} \tag{3.33}$$

$$\dot{\sigma}_{13} = i\left[-\sigma_{12}\Omega^*_{32} + \sigma_{13}\frac{(E_3 - E_1)}{\hbar} + \sigma^*_{23}\Omega^*_{12} - (\omega_a - \omega_b)\sigma_{13}\right] - (\gamma_{13} + \gamma')\sigma_{13} \tag{3.34}$$

$$\dot{\sigma}_{32} = i\left[(\rho_{22} - \rho_{33})\Omega_{32} + \frac{(E_2 - E_3)}{\hbar}\sigma_{32} - \sigma^*_{13}\Omega_{12} + i\omega_b\sigma_{32}\right] - (\gamma_{23} + \gamma')\sigma_{32} \tag{3.35}$$

We now define the frequency detunings, using $\omega_{21} = \omega_{23} = \omega_0$:

$$\frac{Ei - Ej}{\hbar} = \omega_{ij}, \tag{3.36}$$

$$\delta_a = \omega_a - \omega_0, \tag{3.37}$$

$$\delta_b = \omega_b - \omega_0, \tag{3.38}$$

so the equations will be written as:

$$\dot{\rho_{11}} = i(\sigma_{12}\Omega_{21} - \sigma_{21}\Omega_{12}) - \gamma(\rho_{11} - \rho_{11}^0) + \Gamma_{12}\rho_{22} \tag{3.39}$$

$$\dot{\rho_{22}} = i(\sigma_{21}\Omega_{12} + \sigma_{23}\Omega_{32} - \sigma_{12}\Omega_{21} - \sigma_{32}\Omega_{23}) - (\Gamma_{21} + \Gamma_{23} + \gamma)\rho_{22} \tag{3.40}$$

$$\dot{\rho_{33}} = i(\sigma_{32}\Omega_{23} - \sigma_{23}\Omega_{32}) - \gamma(\rho_{33} - \rho_{33}^0) + \Gamma_{23}\rho_{22} \tag{3.41}$$

$$\dot{\sigma}_{12} = i\left[(\rho_{22} - \rho_{11})\Omega_{12} - \sigma_{13}\Omega_{32}\right] - (i\delta_a + \gamma_{12} + \gamma)\sigma_{12} \tag{3.42}$$

$$\dot{\sigma}_{13} = i\left[-\sigma_{12}\Omega_{32}^* + \sigma_{23}^*\Omega_{12}^*\right] - (i\delta_a - i\delta_b + \gamma_{13} + \gamma)\sigma_{13} \tag{3.43}$$

$$\dot{\sigma}_{32} = i\left[(\rho_{22} - \rho_{33})\Omega_{32} - \sigma_{13}^*\Omega_{12}\right] - (i\delta_b + \gamma_{23} + \gamma)\sigma_{32}. \tag{3.44}$$

Now, we have all of our Bloch equations. We shall then, solve for the coherence between levels $|1\rangle$ and $|2\rangle$, σ_{12}. For this we will use the steady-state solution, where $\dot{\rho}_{ii}$ and $\dot{\sigma}_{ij}$ are zero, giving us the set of equations:

$$\rho_{11} = \frac{i\left[-\sigma_{12}\Omega_{12}^* + \sigma_{12}^*\Omega_{12}\right] + \gamma\rho_{11}^0 + \Gamma_{12}\rho_{22}}{\gamma}, \tag{3.45}$$

$$\rho_{22} = \frac{-i\left[-\sigma_{12}^*\Omega_{12} + \sigma_{12}\Omega_{12}^* - \sigma_{32}^*\Omega_{32} + \sigma_{32}\Omega_{32}^*\right]}{\Gamma_{21} + \Gamma_{23} + \gamma}, \tag{3.46}$$

$$\rho_{33} = \frac{i\left[-\sigma_{32}\Omega_{32}^* + \sigma_{32}^*\Omega_{32}\right] + \gamma\rho_{33}^0 + \Gamma_{23}\rho_{22}}{\gamma}, \tag{3.47}$$

$$\sigma_{12} = \frac{i\left[(\rho_{22} - \rho_{11})\Omega_{12} - \sigma_{13}\Omega_{32}\right]}{i\delta_a + \gamma_{12} + \gamma}, \tag{3.48}$$

$$\sigma_{13} = \frac{i\left[-\sigma_{12}\Omega_{32}^* + \sigma_{32}^*\Omega_{12}\right]}{i\delta_a - i\delta_b + \gamma_{13} + \gamma}, \tag{3.49}$$

$$\sigma_{32} = \frac{i\left[(\rho_{22} - \rho_{33})\Omega_{32} - \sigma_{13}^*\Omega_{12}\right]}{i\delta_b + \gamma_{23} + \gamma}. \tag{3.50}$$

As we measure intensity, the FWM signal will be given by the $|\sigma_{12}|^2$. To solve for it, we must first solve for σ_{13}:

$$\sigma_{13}(i\delta_a - i\delta_b + \gamma_{13} + \gamma') = i\left[-\Omega_{32}^*\frac{(\rho_{22} - \rho_{22})\Omega_{12} - \sigma_{13}\Omega_{32}}{i\delta_a + \gamma_{12} + \gamma'} + \Omega_{12}\frac{(\rho_{33} - \rho_{22})\Omega_{32}^* + \sigma_{13}\Omega_{12}^*}{-i\delta_b + \gamma_{23} + \gamma'}\right],$$

$$\sigma_{13} = \frac{\Omega_{32}^*\Omega_{12}\left[\frac{\rho_{22}-\rho_{11}}{i\delta_a+\gamma_{12}+\gamma'} - \frac{\rho_{33}-\rho_{22}}{-i\delta_b+\gamma_{23}+\gamma'}\right]}{i(\delta_a - \delta_b) + \gamma' + \gamma_{13} + \frac{|\Omega_{32}|^2}{i\delta_a+\gamma_{12}+\gamma'} + \frac{|\Omega_{12}|^2}{-i\delta_b+\gamma_{23}+\gamma'}}. \tag{3.51}$$

Substituting eq. 3.51 in eq. 3.48:

$$\sigma_{12} = \frac{1}{i\delta_a + \gamma_1 2 + \gamma'} \times \left[i(\rho_{22} - \rho_{11})\Omega_{12} + \frac{\Omega_{32}\Omega_{32}^*\Omega_{12}\left[\frac{\rho_{22}-\rho_{11}}{i\delta_a+\gamma_{12}+\gamma'} - \frac{\rho_{33}-\rho_{22}}{-i\delta_b+\gamma_{23}+\gamma'}\right]}{i(\delta_a - \delta_b) + \gamma' + \gamma_{13} + \frac{|\Omega_{32}|^2}{i\delta_a+\gamma_{12}+\gamma'} + \frac{|\Omega_{12}|^2}{-i\delta_b+\gamma_{23}+\gamma'}}\right]. \tag{3.52}$$

Due to Doppler-broadening it is necessary to integrate this equation in a Maxwell-Boltzmann velocity distribution. To integrate in velocity, and get figure 24 (b) we used a Mathematica program, shown in appendix A. We did not considerate the first term of equation 3.52, the propagation term. Typically, FWM processes are investigated when one laser has a fixed frequency and the frequency of the other one is swept, as showed by (ALVAREZ; ALMEIDA; VIANNA, 2021), where $\delta_a = 0$ and δ_b varying or vice versa. In our case, we use a single laser, and the resulting signal, for $\delta_a = \delta_b$ varying together is shown in figure 24 (b). Figure 24 (a) shows us the FWM signal for only one velocity group, without integrating in velocity. Figure 24 (b) shows us the expected result, a large Gaussian shaped peak (XUE-MEI et al., 2012), due to Doppler effect.

In figures 24 and 25 we have the calculated four wave mixing signal versus the frequency detuning. We can see in part (a) of figure 24 and in figure 25 that there is a power broadening. This broadening is due to the terms that go with the square of Rabi's frequency in the denominator of the second term of equation 3.52. However, when we do velocity integration, we cannot see the power broadening in the system response since the Doppler broadening is much greater than the power broadening, as seen in part (b) of figure 24. In figure 26 we see the same power broadening, but for only one beam varying in frequency. In this case, more commom on literature, the power broadening is more clear.

To get the peak structure that we observed, we would have to use a more complicated model, probably with another excited level to take into account other hyperfine excited states and another ground state, to consider optical pumping effects. We also need to take into account propagation effects, given by the first term of equation 3.52. Unfortunately, we did not have time to continue this calculation.

Figure 24 – The FWM signal ($|\sigma_{12}|^2$) by the frequency detuning: (a) without integrating in velocities and (b) with integration in velocities. All curves are normalized.

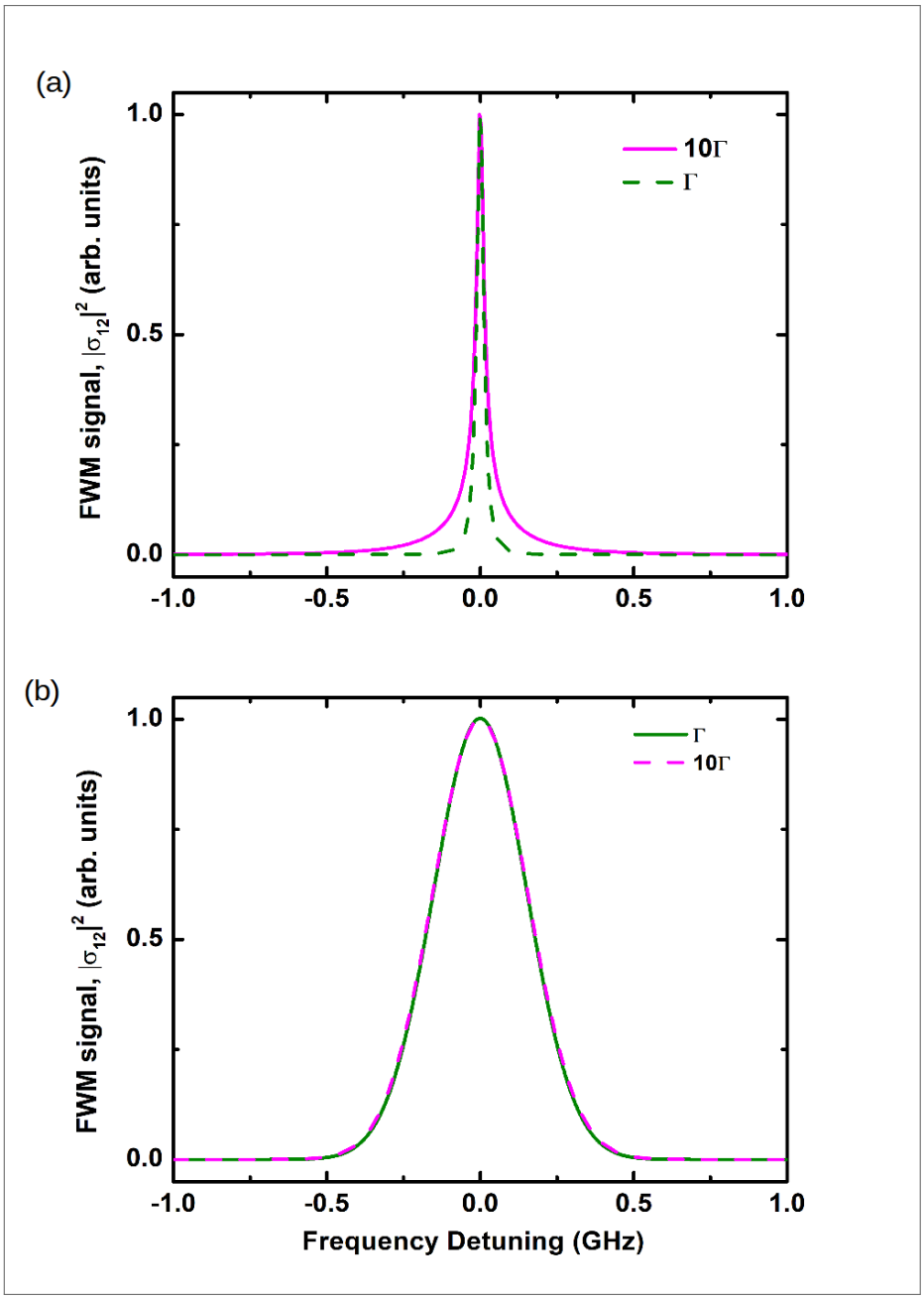

Source: the author (2024)

Figure 25 – Four wave mixing signal for two beams varying in frequency for different intensities. This is the same as figure 24 (a) but with a zoom. We can see more clearly that for the higher intensity there is a discrete broadening in the signal.

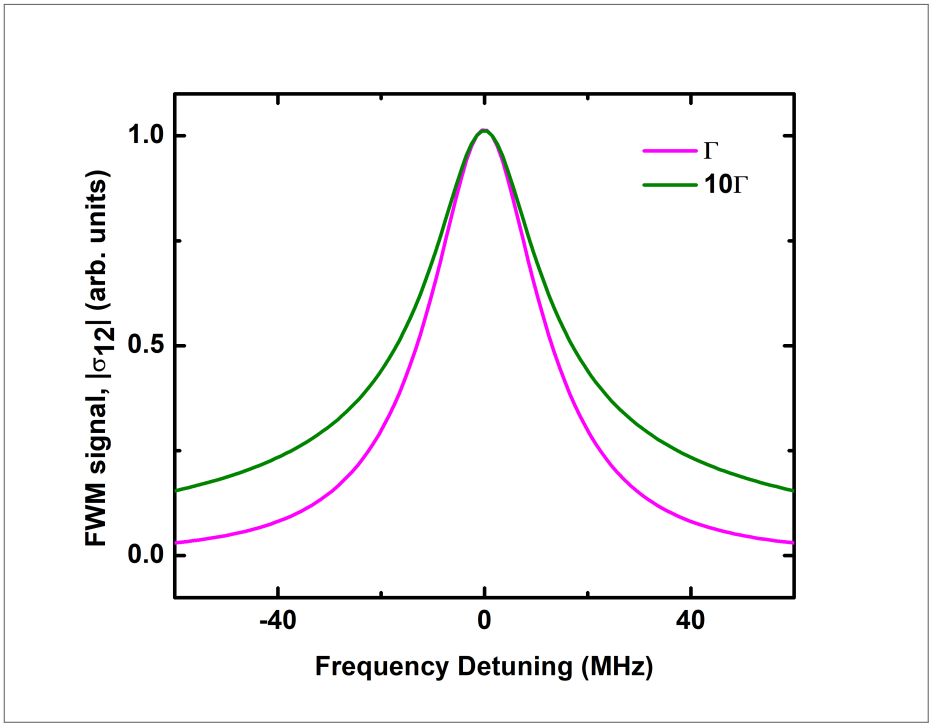

Source: the author (2024)

Figure 26 – Four wave mixing signal for one beam varying in frequency and the other with fixed frequency for different intensities. We can see that for the higher intensity there is a discrete broadening in the signal.

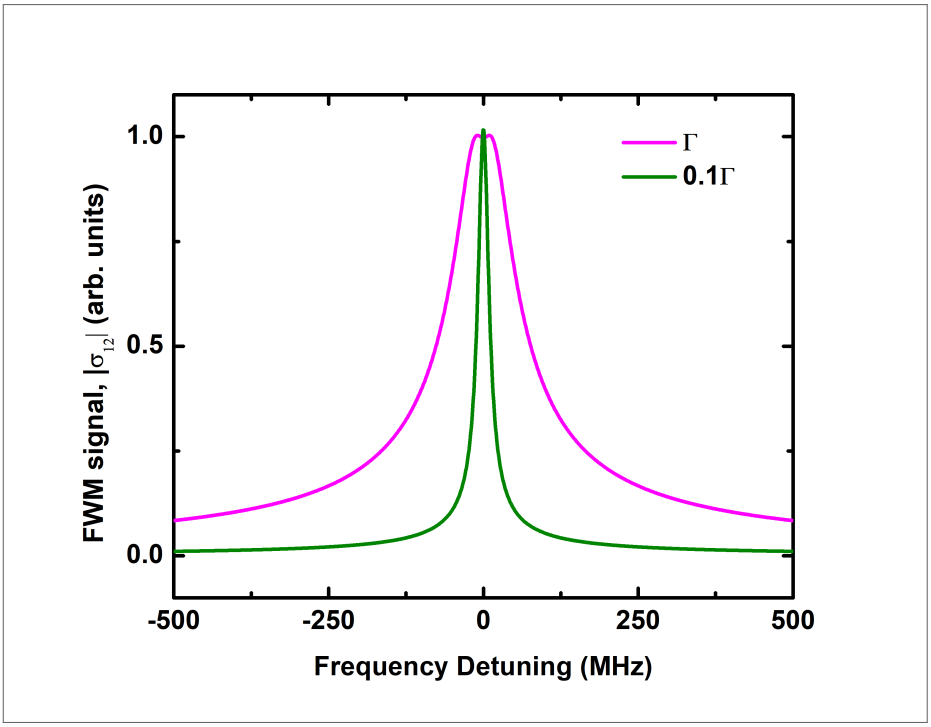

Source: the author (2024)

3.2 THE FOUR WAVE MIXING EXPERIMENT

In figure 27 we can see the experimental setup for the FWM, which is very similar to the setup used to observe the Faraday effect. Comparing figures 11 and 27 we see that the two setups are identical from the diode laser until PBS 1. This PBS 1 divide the laser beam in two beams with linear orthogonal polarizations. We call beam a the beam which is transmitted by the PBS 1 and beam b the reflected one. Beams a and b go through different ways until they meet again in PBS 2. We align beams a and b so that they cross each other about the center of the cell. The four wave mixing signals are generated due to the interaction of the two incident beams with the Rb atoms. After the sample we have then four beams: the two transmitted incident beams a and b and the two generated FWM signals at the directions $2\vec{k_b} - \vec{k_a}$ and $2\vec{k_a} - \vec{k_b}$. We first separate the beams using PBS 3, since the 2a-b beam has the same polarization as beam b and 2b-a beam has the same polarization as beam a. In the last step, we separate beams of the same polarization spatially, placing the detector far from the sample, since there is a small angle, of about 10 mrad, between the beams. To predict the direction of the beams we use a guide mask, as shown in figure 28. We make a guide beam pass through the first hole in mask 1 and the fourth hole in mask 2, in such a way we can align the detector in the expected direction of the generated beam 2b-a. For looking into the influence of the geomagnetic field into the FWM signal we used a magnetic shield, like in figure 13. Most of our measurements were made without the magnetic shield, when it was used it is indicated.

Figure 27 – Experimental setup for the FWM measurements

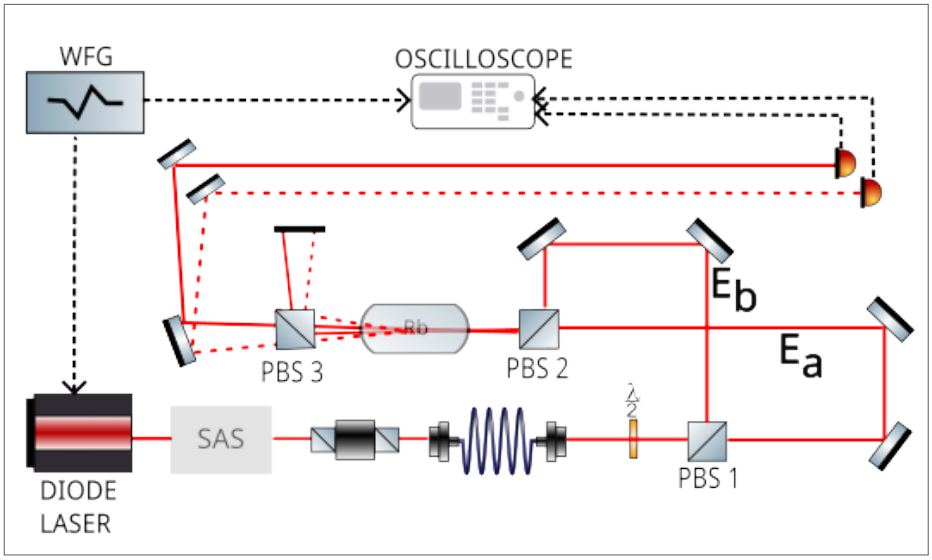

Source: the author (2024)

Figure 28 – The 4 beams passing through the guide mask. The incident beams are the ones in solid line while the guide beams are on dashed line.

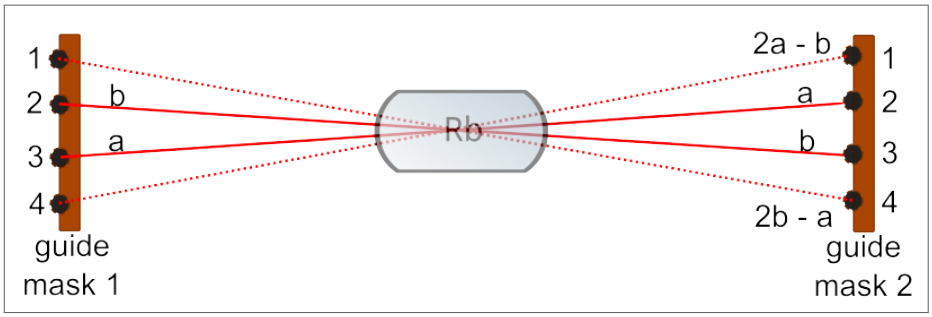

Source: the author (2024)

3.3 RESULTS

In this section, we discuss the results of the FWM experiment. The experiment was performed for different temperatures, with and without a magnetic shield and for various intensities varying in the range of about 100 to 1000 times the saturation intensity. The saturation intensity is the light intensity at which the rate of excitation of atoms or molecules to a higher energy level by the light matches the rate at which they spontaneously return to a lower energy level.

In figures 29 and 30 we see that when the ground states are the $^{87}Rb,\ F_g = 1$ and $^{85}Rb,\ F_g = 2$ the FWM signal was not observed for the range of intensities used, so we decided to focus our studies at the other two hyperfine states, $^{87}Rb,\ F_g = 2$ and $^{85}Rb,\ F_g = 3$. We can also see

(figure 30) that there is a peak structure in each Doppler of the FWM signal. This structure is not in the Gaussian shape expected, as the simple theoretical model of a three level system suggested (figure 24).

Figure 29 – FWM signal versus the frequency detuning. The FWM signal is only observed for hyperfine levels ^{87}Rb, $F_g = 2$ and ^{85}Rb, $F_g = 3$.

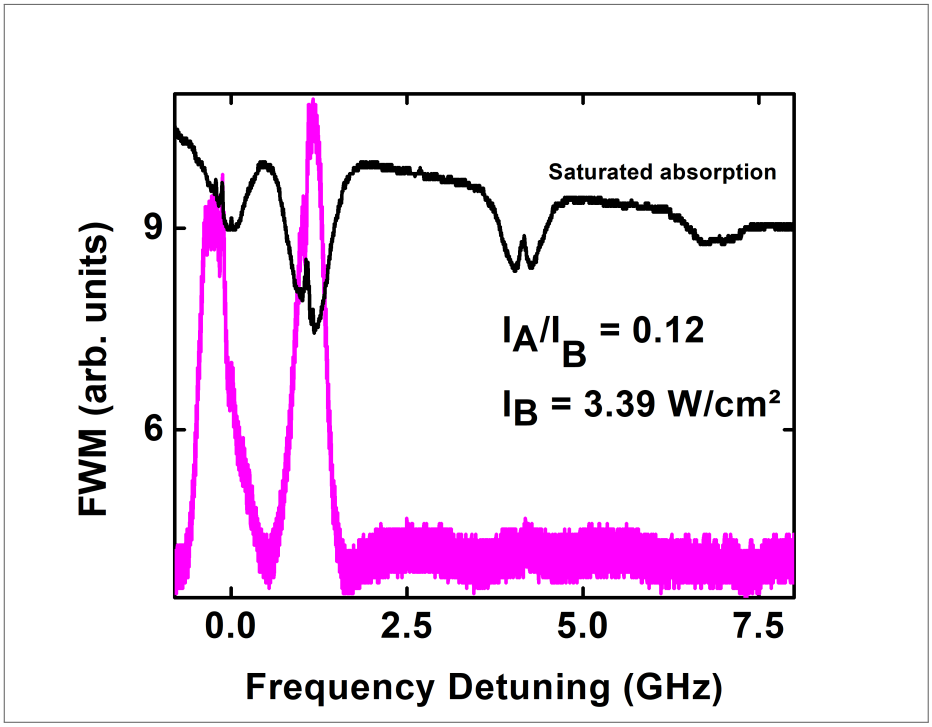

Source: the author (2024)

Since we observed a Faraday rotation in the transmitted beam due to the geomagnetic field we decided to investigate if the FWM signal was also influenced by this external magnetic field. Figure 31 shows the SA curve, a green curve, that corresponds to the FWM signal obtained without the magnetic shield, and a pink curve, that shows the FWM signal obtained with a magnetic shield around the cell, as shown in figure 13. Both FWM signals, obtained with and without the magnetic shield, are very similar, suggesting that the observed peak structure is not due to the magnetic field of the Earth.

Figure 32 shows our results for different intensity ratios. The pink curve is the same for both figures 32 (a) and (b). The intensity of beam b was kept at 350 mW/cm^2 while we varied the intensity of beam a. In these figures there are two interesting behaviors. In the ^{87}Rb, $F_g = 2$ Doppler, the green curve, for an intensity ratio of 0.003, we have a softer curve, without any peaks, as we increase the ratio the peak structure becomes more evident. We can also notice in this Doppler that the relative intensity between the peaks varies with the ratio.

Figure 30 – FWM signal versus the frequency detuning.

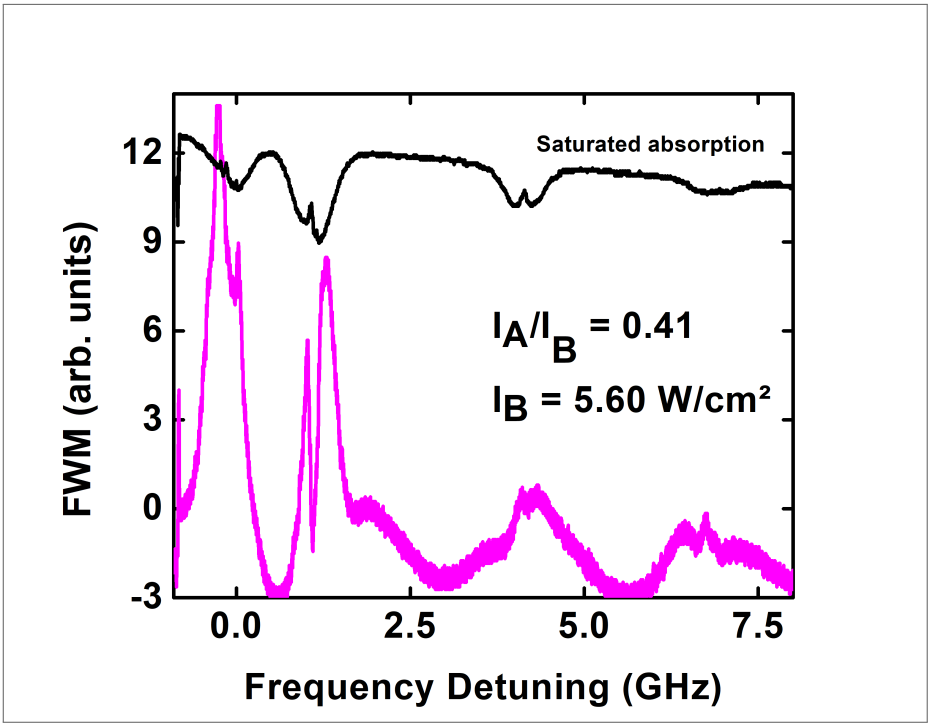

Source: the author (2024)

In the ^{85}Rb, $F_g = 3$ Doppler the peak structure also becomes more evident, and as $I_a/I_b \to 1$, the observed structure becomes a large dip.

One could expect that this dip is due to an absorption effect, that increases with temperature (and thus atomic density). However, as we can see in figure 33, that is not the case. In this figure we have curves for three different temperatures: 72 ºC, 62 ºC and 53 ºC, for similar intensity ratios. The dip is present in all three curves but is deeper in the blue curve, for 53ºC and the depth decreases as the temperature increases, suggesting that the existence of the dip is not due to an absorption effect.

A similar behavior, with the FWM spectrum strongly dependent on the intensity of the driven fields, was described in (SILANS et al., 2011), using a degenerated backward FWM configuration. In this case, when the pump power is increased, the intensity of the conjugated signal at resonances and crossover changes from a peak to a dip. For high pump powers, they observe a spectrum very similar to what we obtain, a broadened signal with dips in resonances and crossovers. In this case, the explanation for the broadened signal comes from large Stark shifts induced by the pump beams at resonances and the dip formation from some saturation effect.

In figure 34 we have a reproduction of the curves with intensity ratios $I_a/I_b = 0.1$ (a) and

Figure 31 – FWM signal versus the frequency detuning for the ^{87}Rb, $F_g = 2$ and ^{85}Rb, $F_g = 3$ transitions. The green curve shows the FWM signal in the presence of the geomagnetic field and the pink curve was obtained with a magnetic shield.

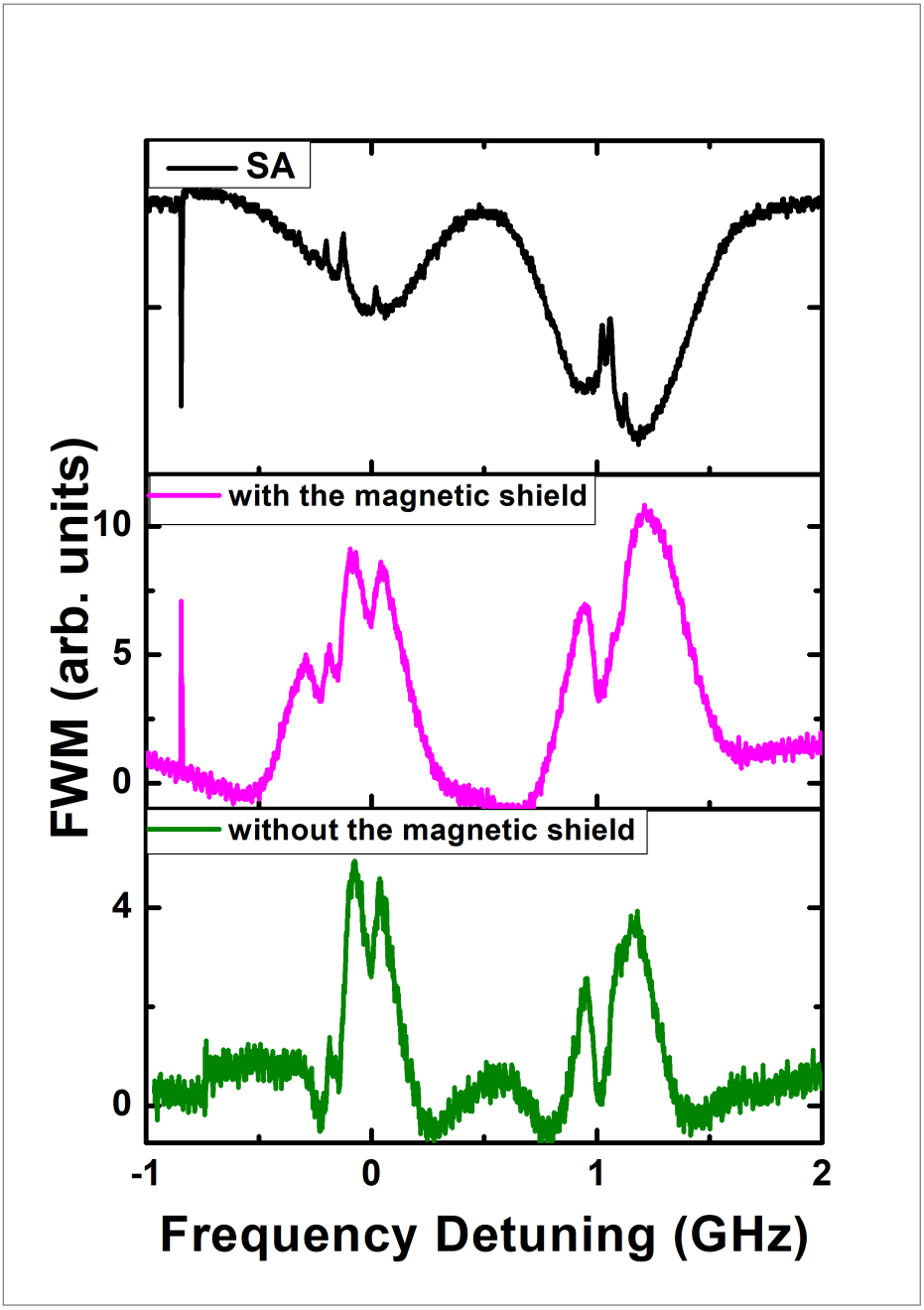

Source: the author (2024)

$I_a/I_b = 1$ (b) of figure 32. The coloured line shows the FWM signal versus frequency detuning while the black line shows us the saturated absorption. As we can see from the dashed lines in figure 34 (a), we have dips in the peaks of the saturated absorption. These dips are located at the position of the cyclic transition, the ones more to the right in each Gaussian curve, and, at the position of the crossover peaks, the ones more to the left of each Gaussian curve. In figure 34 (b), when the intensity ratio is 1, the ^{85}Rb Gaussian has a single large dip. This

Figure 32 – FWM signal versus the frequency detuning for the ^{87}Rb $F_g = 2$ and ^{85}Rb $F_g = 3$ transitions. Each curve shows the FWM signal for a different intensity ratio for $I_b = 350$ mW/cm^2 (a) for lower intensity ratios and (b) for higher intensity ratios.

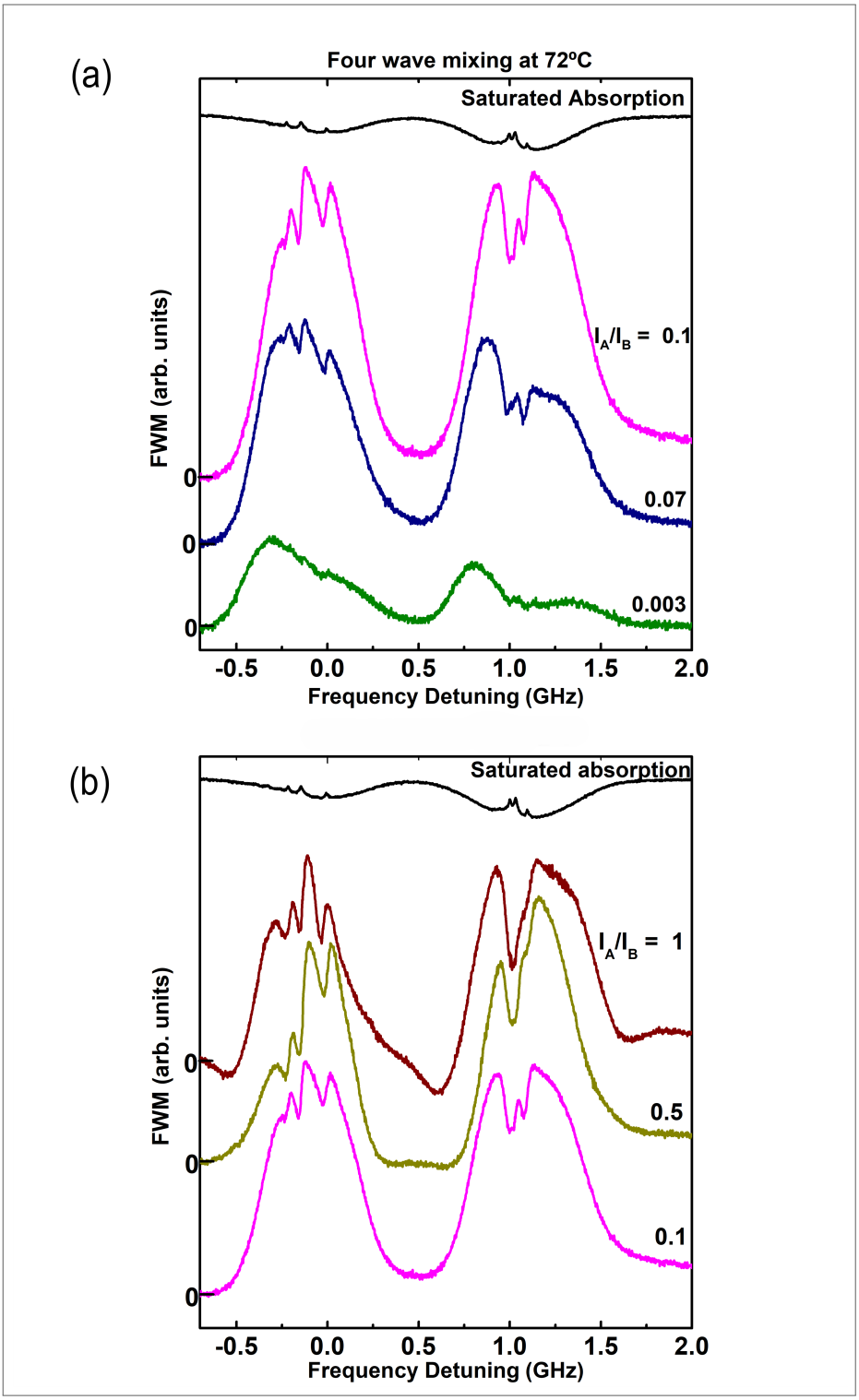

Source: the author (2024)

likely occurs for two reasons: an enlargement caused by high intensity, and the fact that the transitions are very close together, potentially overlapping due to the high intensity.

Figure 33 – FWM versus the frequency detuning for the $^{87}Rb,\ F_g = 2$ and $^{85}Rb,\ F_g = 3$ transitions. Each curve shows the FWM signal for a different temperature and similar intensity ratios. $I_a/I_b \approx 0.5$

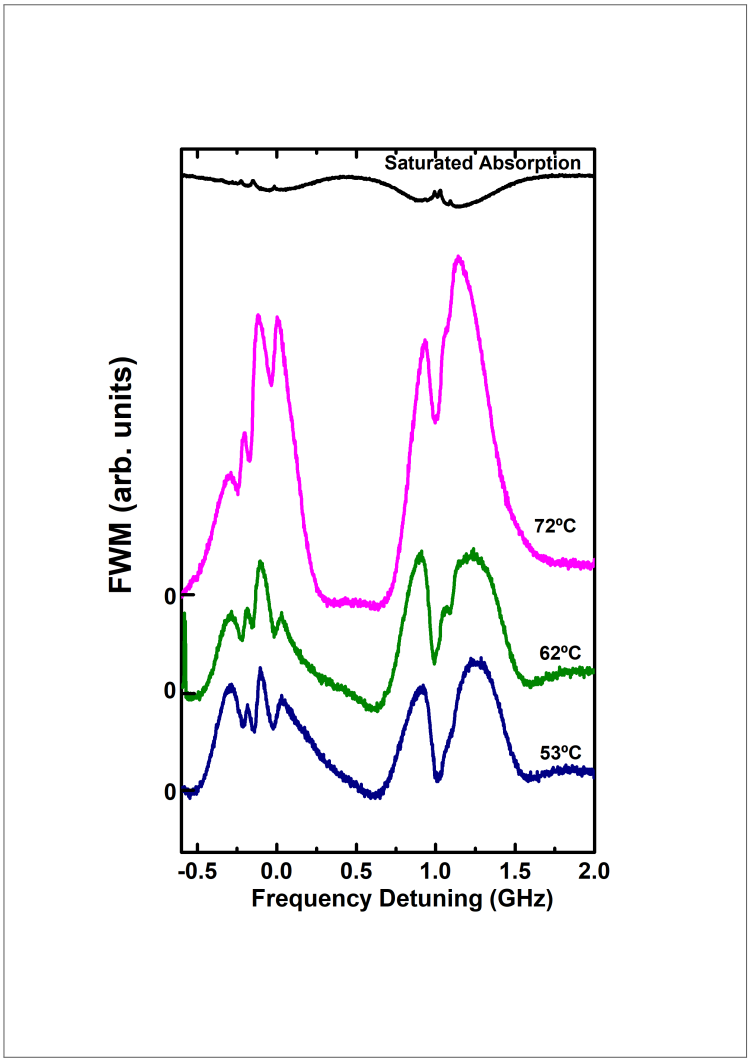

Source: the author (2024)

Our FWM experiment used a co-propagating beams configuration and explored different conditions, including changes in temperature, the presence or absence of a magnetic shield, and varying light intensities from 100 to 1000 times the saturation intensity. Overall, our results show that FWM signals depend on a complex interplay of atomic states, intensity ratios, and temperature. This complexity suggests that we need more detailed models to fully understand the phenomena we have observed.

Figure 34 – FWM signal versus the frequency detuning for the $^{87}Rb\ F_g = 2$ and $^{85}Rb\ F_g = 3$ transitions. (a) For intensity ratio 0.1 and (b) for intensity ratio 1. We can see from the dashed lines that the peaks in the saturated absorption become dips in the FWM signal.

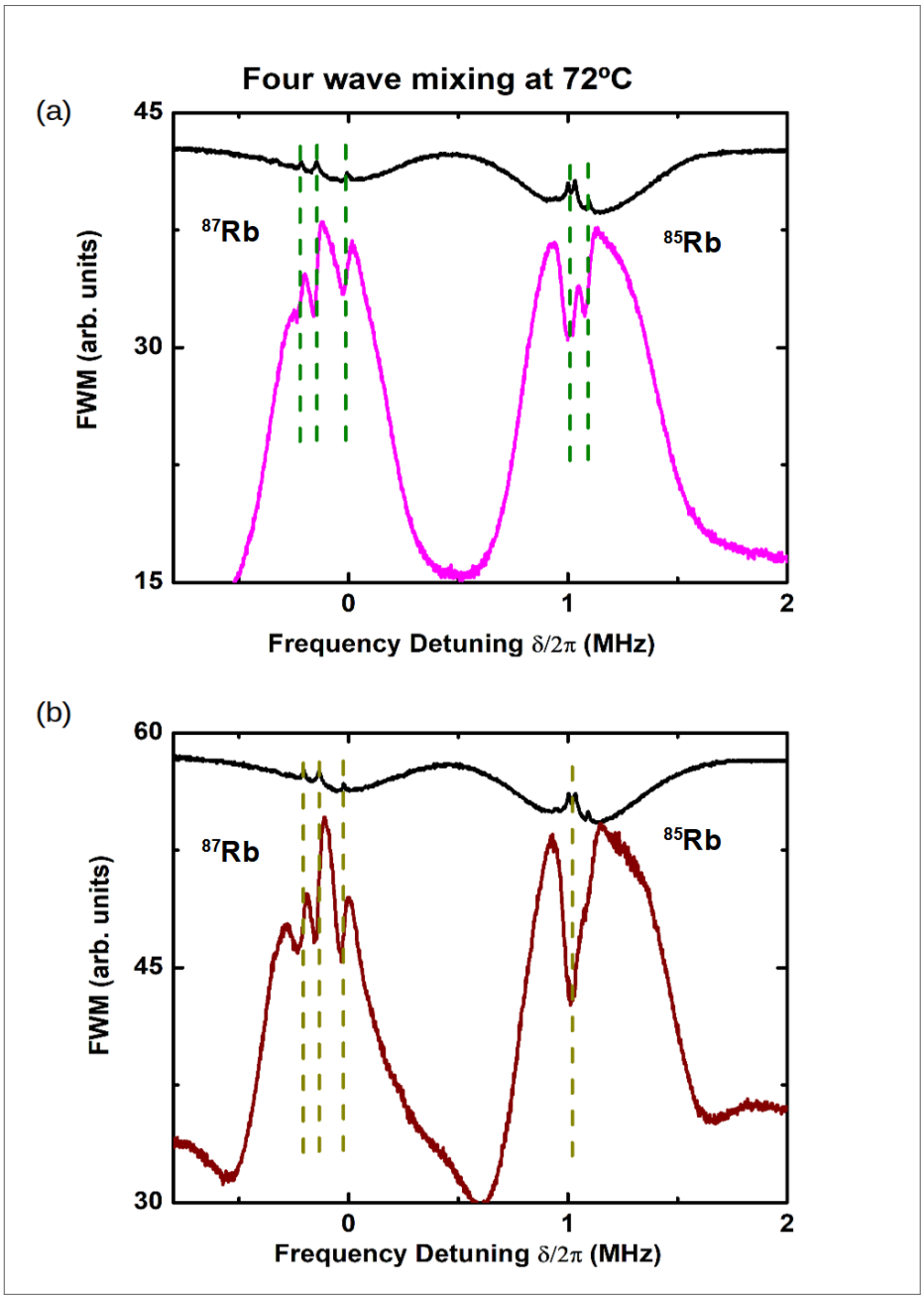

Source: the author (2024)

4 CONCLUSIONS

In this work we have presented experimental results obtained for the FWM signal generated in Rb vapor where the non linear process is driven by a single laser and fields of high intensity. We also investigated the Faraday rotation in the transmitted beam. We have got results for different intensities ratios, different temperatures and with and without a magnetic shield.

For the FWM experiment we have obtained spectra with a peak structure instead of the Gaussian shaped signal predicted by a simple theoretical model. Our results indicate that to theoretically describe this peak structure it will be necessary to consider a more robust model, including a second excited state.

From the different FWM temperatures measurements we have seen that the peak structure is not due to a simple absorption effect, since the dip in the $^{85}Rb, F_g = 3$ decreases when we increase temperature. We also verified that the peak structure was not due to the geomagnetic field. We verified that the external magnetic field does not influence this structure.

The polarization rotation effect observed in the transmitted beam was confirmed to be due to the Faraday effect. For this Faraday rotation we focused our studies in the $^{85}Rb, F_g = 3$ and $^{87}Rb, F_g = 2$ Dopplers, since the rotation for the other two Dopplers were only seen for lower intensities. We suggested that this happens because of an optical pumping that takes the atoms from the levels $^{85}Rb, F_g = 2$ and $^{87}Rb, F_g = 1$ to the $^{85}Rb, F_g = 3$ and $^{87}Rb, F_g = 2$ levels. Using the results from the Faraday rotation experiment we were able to measure the rotation angle as well as obtained the Verdet constant, getting a result with good agreement with values cited in the literature.

We have the perspective to further investigate the peak structure in the FWM, working in a more sophisticated theoretical analysis.

REFERENCES

ALVAREZ, A. S.; ALMEIDA, A. A. C. de; VIANNA, S. S. Two symmetric four-wave mixing signals generated in a medium with anomalous refractive index. *Journal of Physics B: Atomic, Molecular and Optical Physics*, v. 54, p. 045403, 2021. Available at: <https://dx.doi.org/10.1088/1361-6455/abe178>.

ARMSTRONG, J. A.; BLOEMBERGEN, N.; DUCUING, J.; PERSHAN, P. S. Interactions between light waves in a nonlinear dielectric. *Physical Review*, v. 127, p. 1918–1939, 1962. Available at: <https://api.semanticscholar.org/CorpusID:53491675>.

BOYD, R. W. *Nonlinear Optics, Third Edition*. 3rd. ed. [S.l.]: Academic Press, Inc., 2008. ISBN 0123694701.

BOYD, R. W.; RAYMER, M. G.; NARUM, P.; HARTER, D. J. D. Four-wave parametric interactions in a strongly driven two-level system. *Physical Review A*, v. 24, p. 411–423, 1981. Available at: <https://api.semanticscholar.org/CorpusID:121564929>.

BUDKER, D.; GAWLIK, W.; KIMBALL, D. F.; ROCHESTER, S. M.; YASHCHUK, V. V.; WEIS, A. Resonant nonlinear magneto-optical effects in atoms. *Review of Modern Physics*, v. 74, p. 1153–1201, 2002. Available at: <https://link.aps.org/doi/10.1103/RevModPhys.74.1153>.

CHOPINAUD, A.; JACQUEY, M.; LESEGNO, B. Viaris de; PRUVOST, L. High helicity vortex conversion in a rubidium vapor. *Physics Review A*, v. 97, p. 063806, 2018. Available at: <https://link.aps.org/doi/10.1103/PhysRevA.97.063806>.

FARADAY, M. P.; COLLIN, W.; LIBRARY, B. On the magnetization of light and the illumination of magnetic lines of force. *The Royal Society*, 1846. Available at: <https://api.semanticscholar.org/CorpusID:222444786>.

FOOT, C. J. *Atomic Physics*. Oxford University Press, 2004. ISBN 9780198506959. Available at: <https://doi.org/10.1093/oso/9780198506959.001.0001>.

GLORIEUX, Q.; ALADJIDI, T.; LETT, P.; KAISER, R. Hot atomic vapors for nonlinear and quantum optics. *New Journal of Physics*, v. 25, 2023. Available at: <https://iopscience.iop.org/article/10.1088/1367-2630/acce5a>.

JACQUES, V.; HINGANT, B.; ALLAFORT, A.; PIGEARD, M.; ROCH, J. F. Nonlinear spectroscopy of rubidium: an undergraduate experiment. *European Journal of Physics*, v. 30, n. 5, p. 921, 2009. Available at: <https://dx.doi.org/10.1088/0143-0807/30/5/001>.

KATZIR, I.; RON, A.; FIRSTENBERG, O. Diffraction manipulation by four-wave mixing. *Optics Express*, v. 23, p. 6379–6391, 2015.

LABEYRIE, G.; MINIATURA, C.; KAISER, R. Large faraday rotation of resonant light in a cold atomic cloud. *Physics Review A*, v. 64, p. 033402, 2001. Available at: <https://link.aps.org/doi/10.1103/PhysRevA.64.033402>.

MA, R.; LIU, W.; QIN, Z.; SU, X.; JIA, X.; ZHANG, J.; GAO, J. Compact sub-kilohertz low-frequency quantum light source based on four-wave mixing in cesium vapor. *Optics Letters*, v. 43, p. 1243–1246, 2018.

MAIMAN, T. H. Stimulated optical radiation in ruby. *Nature*, v. 187, p. 493–494, 1960. Available at: <https://doi.org/10.1038/187493a0>.

MüLLER-KIRSTEN, H. J. W. *Basics of statistical physics*. 3rd. ed. [S.l.]: World Scientific, 2022. ISBN 9789814449557.

OFFER, R. F.; STULGA, D.; RIIS, E.; FRANKE-ARNOLD, S.; ARNOLD, A. S. Spiral bandwidth of four-wave mixing in rb vapour. *Communications Physics*, v. 1, p. 84, 2018. Available at: <https://doi.org/10.1038/s42005-018-0077-5>.

PATNAIK, A. K.; AGARWAL, G. Coherent control of magneto-optical rotation in inhomogeneously broadened medium. *Optics Communications*, v. 199, p. 127–142, 2001. Available at: <https://www.sciencedirect.com/science/article/pii/S0030401801015346>.

SILANS, T. P. de; GONCALVES, C. S. L.; FELINTO, D.; TABOSA, J. W. R. Enhanced four-wave mixing via crossover resonance in cesium vapor. *J. Opt. Soc. Am. B*, Optica Publishing Group, v. 28, n. 9, p. 2220–2226, Sep 2011. Available at: <https://opg.optica.org/josab/abstract.cfm?URI=josab-28-9-2220>.

STECK, D. Rubidium 87 d line data. 2003. Available at: <https://steck.us/alkalidata/rubidium87numbers.pdf>.

STECK, D. Rubidium 85 d line data. 2007. Available at: <https://steck.us/alkalidata/rubidium85numbers.pdf>.

WELLER, L.; KLEINBACH, K. S.; ZENTILE, M. A.; KNAPPE, S.; HUGHES, I. G.; ADAMS, C. S. Optical isolator using an atomic vapor in the hyperfine paschenback regime. *Optics Letters*, v. 37, p. 3405–3407, 2012. Available at: <https://opg.optica.org/ol/abstract.cfm?URI=ol-37-16-3405>.

WILSON, N. M. *Nonlinear Magneto-Optical Rotation in Rubidium Vapour*. Phd Thesis — School of Physical Sciences, The University of Adelaide, 2020.

XUE-MEI, C.; HAO-WEI, C.; JIAN, W.; YI-ZHU, M.; XUN-LI, Y.; ZHAO-YU, R.; JIN-TAO, B. Resolution for forward and phase-conjugate degenerate four-wave mixing in hot atomic media. *Chinese Physics Letters*, v. 29, p. 074212, 2012. Available at: <https://dx.doi.org/10.1088/0256-307X/29/7/074212>.

ŠKOLNIK, G.; VUJIčIć, N.; BAN, T. Optical pumping of the zeeman components in the rubidium vapor. *Optics Communications*, v. 282, n. 7, p. 1326–1334, 2009. Available at: <https://www.sciencedirect.com/science/article/pii/S0030401808012431>.

APPENDIX A – MATHEMATICA PROGRAM FOR THE THREE LEVEL SYSTEM

```
In[1]:= u = Sqrt[2 * 295 * 1.38 * 10^-23 / (1.443 * 10^-25)] / 10^6;
        raiz quadrada
        Γ = 12.14 * Pi / 2;
                    número pi
        γ = Γ / 100;
        c = 2.99792458 * 10^2;
        ω21 = 2 * Pi * 384 228.116 * 10^3;
                 número pi
        ρ110 = 1 / 2;
        ρ220 = 0;
        ρ330 = 1 / 2;
        Ω23 = 10 * Γ;
        Ω12 = 10 * Γ;
```

```
In[•]:= SetDirectory["C:\\Users\\raiss\\OneDrive\\Nova pasta\\OneDrive\\faculdade"]
        define diretório   símbolo de constante
Out[•]= C:\Users\raiss\OneDrive\Nova pasta\OneDrive\faculdade
```

```
In[11]:= l[δ12_ , δ23_ ] :=
```

$$-\left(\left(\left(i\,\Omega12\,\Omega23\,\Omega23\right)\left(\frac{\frac{\rho110}{1}}{\gamma+\frac{\Gamma}{2}+i\,\delta12}+\frac{\frac{\rho330}{1}}{\gamma+\frac{\Gamma}{2}-i\,\delta23}\right)\right)\Big/\left(\left(\gamma+\frac{\Gamma}{2}+i\,\delta12\right)\left(\frac{\Omega12^2}{\gamma+\frac{\Gamma}{2}+i\,\delta12}+\frac{\Omega23^2}{\gamma+\frac{\Gamma}{2}-i\,\delta23}+\gamma+\frac{\Gamma}{2}+i\,(\delta12-\delta23)\right)\right)\right)-\frac{0*\left(i\,\Omega12\left(\frac{\rho110}{\frac{2\,\Omega12^2\left(\gamma+\frac{\Gamma}{2}\right)(\Gamma+2\gamma)}{(\gamma(\gamma+\Gamma+\Gamma))\left(\left(\gamma+\frac{\Gamma}{2}\right)^2+\delta12^2\right)}+1}\right)\right)}{\gamma+\frac{\Gamma}{2}+i\,\delta12};$$

```
In[•]:= casos = Transpose[
                transposição
          {Table[δ1, {δ1, -50 Γ, 50 Γ, 1}], Table[Abs[l[δ1, δ1]], {δ1, -50 Γ, 50 Γ, 1}] }];
           tabela                                 tabela  valor absoluto
```

```
In[•]:= Export["alargamento_10gamma.csv", casos]
        exporta
Out[•]= alargamento_10gamma.csv
```

```
"alargamento_gamma_delta0.csv"
```

In[12]:=
```
Plot[Abs[l[δ1, δ1]], {δ1, -3 Γ, 3 Γ}, AxesLabel → {δ (MHz), σ12}, PlotRange → All]
```
gráf··· valor absoluto legenda dos eixos intervalo do g··· tudo

Out[12]=

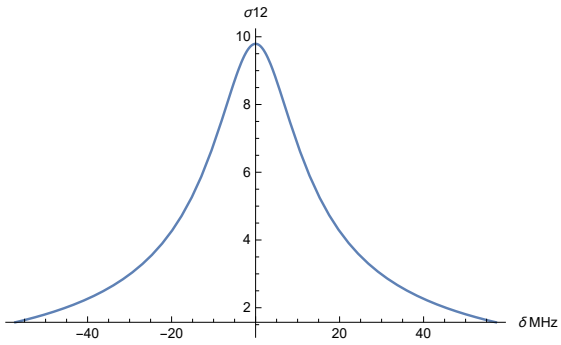

In[13]:=
```
{maxValue, maxPos} = FindMaximum[Re[l[δ12, δ12]], {δ12, -1000, 1000}];
```
encontra o má·· parte real

```
(*Calculate the half of the maximum value*)
halfMax = maxValue / 2;

(*Define a function for the half maximum*)
fHalfMax[δ12_] := Re[l[δ12, δ12]] - halfMax;
```
parte real

```
(*Solve for the values of δ12 where l[δ12,δ23] equals halfMax*)
```
resolve
```
(*Use real parts and valid range*)
root1 =
  FindRoot[fHalfMax[δ12] == 0, {δ12, -1000, 0}, MaxIterations → 100, AccuracyGoal → 6];
```
encontra raiz número máximo de iteraç··· meta de exatidão
```
root2 = FindRoot[fHalfMax[δ12] == 0, {δ12, 0, 1000},
```
encontra raiz
```
   MaxIterations → 100, AccuracyGoal → 6];
```
número máximo de iteraç··· meta de exatidão
```
(*Calculate the Full Width at Half Maximum (FWHM)*)
```
completo
```
fwhm = Abs[root2[[1, 2]] - root1[[1, 2]]];
```
valor absoluto
```
(*Output the FWHM*)
fwhm
```

Out[19]= 33.0278

In[20]:=
```
Qi = Transpose[{Table[δ, {δ, -1000, 1000, 1}],
    Table[NIntegrate[1[2 Pi δ - ω21 * v * 10^-6 / c, 2 Pi δ - ω21 * v * 10^-6 / c] *
      (1 / (u Sqrt[π]) * Exp[-((v - δ * c / ω21) * 10^-6)^2 / u^2]),
     {v, -Infinity, Infinity}, Method → "LocalAdaptive"] *
    NIntegrate[Conjugate[1[2 Pi δ - ω21 * v * 10^-6 / c, 2 Pi δ - ω21 * v * 10^-6 / c]] *
      (1 / (u Sqrt[π]) * Exp[-((v - δ * c / ω21) * 10^-6)^2 / u^2]), {v, -Infinity,
      Infinity}, Method → "LocalAdaptive"] // Re, {δ, -1000, 1000, 1}]};
```

In[22]:=
```
ListPlot[Qi, Joined → True, AxesLabel → {δ (MHz), σ12}, PlotRange → Automatic]
```

Out[22]=

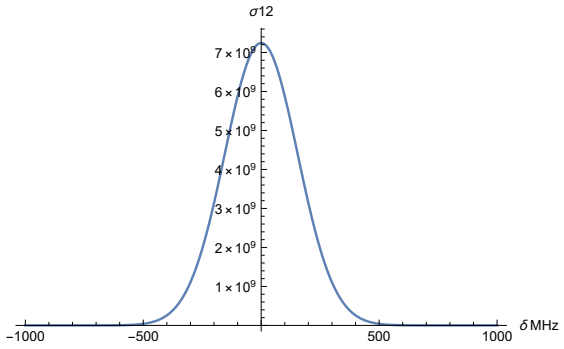

In[23]:=
```
(*Find the maximum value in the data*)
maxValue = Max[Qi[[All, 2]]];

(*Calculate half of the maximum value*)
halfMax = maxValue / 2;

(*Interpolate the data within the valid range*)
interpFunc = Interpolation[Qi];

(*Find the approximate X-range of the data*)
xMin = Min[Qi[[All, 1]]];
xMax = Max[Qi[[All, 1]]];

(*Use FindRoot to find the X-values where the data crosses halfMax*)
root1 = FindRoot[interpFunc[x] == halfMax,
   {x, xMin, (xMin + xMax) / 2}, MaxIterations → 100, AccuracyGoal → 6];
root2 = FindRoot[interpFunc[x] == halfMax, {x, (xMin + xMax) / 2, xMax},
   MaxIterations → 100, AccuracyGoal → 6];

(*Step 6:Calculate the FWHM as the distance between the two roots*)
fwhm = Abs[root2[[1, 2]] - root1[[1, 2]]];

(*Output the FWHM*)
fwhm
```

Out[31]= 364.148